Sustainable Energy & Fuels

Interdisciplinary research for the development of sustainable energy technologies

Accepted Manuscript

This article can be cited before page numbers have been issued, to do this please use: X. Tian, Y. Zhang, R. Zheng, D. Wei and J. Liu, *Sustainable Energy Fuels*, 2020, DOI: 10.1039/C9SE01181A.

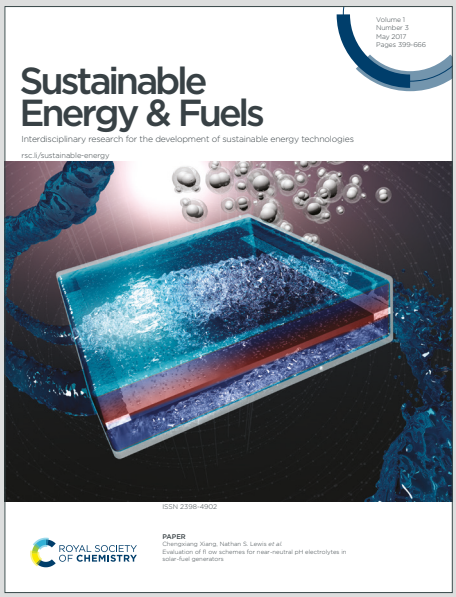

This is an Accepted Manuscript, which has been through the Royal Society of Chemistry peer review process and has been accepted for publication.

Accepted Manuscripts are published online shortly after acceptance, before technical editing, formatting and proof reading. Using this free service, authors can make their results available to the community, in citable form, before we publish the edited article. We will replace this Accepted Manuscript with the edited and formatted Advance Article as soon as it is available.

You can find more information about Accepted Manuscripts in the Information for Authors.

Please note that technical editing may introduce minor changes to the text and/or graphics, which may alter content. The journal's standard Terms & Conditions and the Ethical guidelines still apply. In no event shall the Royal Society of Chemistry be held responsible for any errors or omissions in this Accepted Manuscript or any consequences arising from the use of any information it contains.

View Article Online
DOI: 10.1039/C9SE01181A

ARTICLE

Two-dimensional Organic–Inorganic Hybrid Ruddlesden–Popper Perovskite Materials: Preparation, Enhanced stability, and Applications in Photodetection

Received 00th January 20xx,
Accepted 00th January 20xx

DOI: 10.1039/x0xx00000x

Xiangxin Tian,*[a] Yongzhuan Zhang,*[a] Rongkun Zheng,[b] Di Wei,[c] and Jingquan Liu*[a]

Abstract: Three-dimensional (3D) inorganic–organic hybrid perovskites have attracted considerable attention during the past decade because of their superior optoelectronic properties and broad application prospects, especially in energy-related fields. However, the applications of 3D perovskites, for example, the well-studied $CH_3NH_3PbI_3$, are severely restrained by their environmental instability, photoinstability, and crystal processing difficulties. In contrast to their 3D counterparts, Ruddlesden–Popper phases, which are layered two-dimensional (2D) perovskites, have shown promising stability and excellent performance in photodetection and solar cell applications, which can be achieved through appropriate selection of the organic spacer cations and artificial tuning of the number of perovskite-like layers. Because of their decreased dimensions, novel properties also appear in Ruddlesden–Popper perovskites, such as large exciton binding energy, sensitive photodetection, high photoluminescence quantum yield, and wide bandgap. In light of this, 2D Ruddlesden–Popper perovskites have garnered much interest in recent years and various methods have been developed for their synthesis, property evaluation, and device fabrication. In this review, recent progress in the synthesis and enhanced ambient stability of 2D Ruddlesden–Popper perovskites are summarized. The applications of these materials in advanced photodetectors are emphasized and challenges limiting their ongoing development are also discussed.

1. Introduction

Organic–inorganic hybrid perovskites have drawn unprecedented research interest since the first report of the use of methylammonium ($CH_3NH_3^+$, MA^+) lead halides (methylammonium lead iodide ($MAPbI_3$) and methylammonium lead bromide ($MAPbBr_3$)) in photovoltaic cells by Kojima et al.[1] in 2009. After ten years of rapid development, the power conversion efficiency (PCE) of organic–inorganic hybrid metal halide perovskite solar cells has increased from the initial 3.8% to an astonishing 25.2%, rendering them the most attractive candidates for next-generation photovoltaic technologies.[2-6] In addition, hybrid perovskites also exhibit outstanding application potential in other optoelectronic fields, including highly efficient photodetectors,[7-11] light-emitting diodes,[12-16] and field-effect transistors,[17-20] because of their remarkable features such as bandgap tunability,[21-23] low trap density,[24, 25] high carrier mobility,[26-29] long carrier diffusion lengths,[30-34] and high external quantum efficiencies (EQE) and coefficients.[35, 36] Numerous theoretical studies have also been conducted and provided many inspiring strategies for the design of novel photoelectronic devices based on various perovskites.[37-43] With all these merits, organic–inorganic hybrid perovskites have become a research hot spot in materials science, chemistry, and other related scientific fields in the past decade.

Despite their advantages, there are still some fatal drawbacks hampering the practical deployment of perovskite materials. The two most serious problems limiting perovskites are their poor stability towards environmental moisture and the toxicity of the water-soluble source of lead. The latter problem can potentially be solved by replacing the toxic lead with more environmentally friendly elements like tin.[44-46] However, the improvement of moisture resistance usually requires much more complex modification techniques. For example, the most common perovskite $MAPbI_3$ is intrinsically vulnerable to various environmental conditions, like moisture, light, and heat.[47] To solve this problem, multiple strategies have been proposed and systematically investigated. For instance, the most immediate solution to limit the humidity is to encapsulate the whole device,[48-50] which is effective but leads to complex device structure and increased fabrication cost. In addition, strategies like modifying the perovskite surface with hydrophobic tertiary or quaternary alkylammonium cations as efficient water-resisting layers,[51] modifying the perovskites with ligands or mixed cations,[4, 47, 52] or using an aliphatic fluorinated amphiphilic additive to enhance the stability and performance of the perovskite solar cells at the same time[53] have been investigated. Modification of the structure of perovskite solar cells is also a feasible

[a] School of Materials Science and Engineering, Linyi University, Linyi, 276000, Shandong, China. E-mail: tianxiangxin@lyu.edu.cn, jliu@qdu.edu.cn
[b] School of Physics, The University of Sydney, NSW, 2006, Australia
[c] Beijing Graphene Institute

approach to improve device stability.[54, 55] However, all of these modification and encapsulation strategies increase structural complexity and/or degrade performance.

Recently, two-dimensional (2D) perovskite-like materials, including Ruddlesden–Popper (RP) phases, Dion–Jacobson phases,[56-59] and double perovskite phases,[60-64] have attracted tremendous attention because of their unique crystallographic structural characteristics and promise in energy-related applications. Among quasi-2D perovskites, the RP ones have shown enhanced long-term stability and achieved an acceptable PCE (>13%)[65]. In 2014, the 2D RP perovskite $(PEA)_2(MA)_2Pb_3I_{10}$ (PEA = $C_6H_5(CH_2)_2NH_3^+$) was used as an absorber in a solar cell that achieved an open-circuit voltage of 1.18 V and PCE of 4.73%. Since then, tremendous research effort has been expended and the PCE of a $(C_6H_5CH_2NH_3)_2(FA)_8Pb_9I_{28}$-based device has already reached 17.40%.[66, 67] RP perovskites exhibit strong light absorption in the visible region, accompanied by strong photoluminescence (PL) at room temperature, rendering them promising light absorbers for photovoltaic applications[68]. In addition, the intergrowth of large organic spacer layers and the perovskite-like layers endow RP materials with other unique advantages, like high ambient, structural, and thermal stability as well as attractive structure–property tunability.

Apart from solar cells, RP phases have also drawn considerable attention from photodetection and light-emission researchers. While RP phases exhibit some excellent characteristics, they are not ideal materials. Although the relatively large organic spacers in RP phases help to protect them from moisture, they also lead to strong quantum and dielectric confinement, which widen the optical band gap and decrease the carrier mobility compared with those of three-dimensional (3D) perovskites.[69-71] According to theoretical calculations, the exciton-binding energies of RP perovskites increase as the number of layers decreases, indicating that ultrathin 2D perovskites may be more suitable materials for light emission and photodetection than solar absorbers.[70, 71] Herein, the current main focus of the study of RP phases is to find an ideal trade-off between their ambient stability and charge-carrier mobilities, yielding humidity-resistant materials for highly efficient photoelectronic devices.

In this review, we focus on the recent progress in the development of RP phases, especially in the crystallographic structure, synthesis, single-crystal growth, and enhanced ambient stability. The applications of RP perovskites in highly efficient photodetectors are also discussed.

2. Crystal structure of 2D Ruddlesden–Popper perovskites

The term perovskite was originally used to refer to the mineral calcium titanate but its meaning has since broadened to represent a class of materials with similar crystal structure to that of calcium titanate. Now, a perovskite is a material with a general formula of ABX_3, in which A is a monovalent amine cation , such as MA^+ or $CH(NH_2)_2^+$ (FA^+); B is a bivalent metal cation such as Pb^{2+}, Sn^{2+}, or Mn^{2+}; and X is a monovalent halogen anion like I^-, Cl^-, or Br^-. Perfect perovskite structure has strict crystallographic limitations, in which B and X form regular octahedral BX_6 anionic groups and all the groups are connected together by sharing the common vertex atoms with A cation is located within each four BX_6 octahedra, as illustrated in Fig. 1a. However, in actual compounds, the B cations are sometimes distorted from the center of the octahedra because of the second-order Jahn–Teller effect. Additionally, tilting or rotation of the BX_6 octahedra also give rise to the formation of distorted perovskite structures.[72-74] To better understand the structures of perovskites and describe their evolution, the following empirical formula has been proposed[75, 76]:

$$t = \frac{\left(r_A + r_X\right)}{\sqrt{2}\left(r_B + r_X\right)}, \quad (1)$$

where t is the tolerance factor and r_A, r_B, and r_X represent the radii of A, B, and X, respectively. A t value of 0.9–1 is compatible with ideal cubic perovskite structure, as shown in Fig. 1a. When a small A or large B cation is used and t is in the range of 0.7–0.9, an orthorhombic, rhombohedral, or tetragonal structure usually forms. For the most intensely investigated organic lead halide perovskite $CH_3NH_3PbI_3$, the ionic radii of Pb^{2+}, I^-, and $CH_3NH_3^+$ are 0.132, 0.206, and 0.18 nm, respectively.[77] According to eqn (1), t of $CH_3NH_3PbI_3$ is calculated to be 0.81, corresponding to a distorted non-cubic structure, which is consistent with the experimentally observed tetragonal structure of a well-developed singe crystal.[78] In contrast, when a large A cation is used, t becomes larger than 1, the perovskite structure becomes unstable, and layered perovskites, for example, RP, Dion–Jacobson, and Aurivillius phases, will be obtained. The relationship between t and crystal structure is summarized in Table 1.

Table 1 Tolerance factors of perovskite structures[75]

Tolerance factor	Structure	Comment
<0.7		
0.7-0.9	Tetragonal/orthorhombic/rhombohedral	A too small or B too large
0.9-1.0	Cubic	Ideal perovskite structure
>1.0	Various layered structures	A cation too large

Perovskites, for example, the representative $CH_3NH_3PbI_3$, have been investigated extensively because of their excellent performance in solar cells. However, their use is limited by their poor long-term stability in air. Recent research achievements have suggested that 2D RP-type perovskites usually exhibit high environmental stability. RP perovskites were first characterized by Ruddlesden and Popper in 1957 and are K_2NiF_4-type all-inorganic layered perovskites with an empirical formula that can be expressed as $A_{n+1}B_nO_{3n+1}$ or $(AO)(A_nB_nO_{3n})$ (where $n \geq 1$ and represents the number of octahedral layers in the perovskite-like stack)[79]. Figure 1b shows that all-inorganic RP perovskites exhibit distinct structural features with the intergrowth of perovskite-like layers ($A_nB_nO_{3n}$) and rock-salt layers (AO).

View Article Online
DOI: 10.1039/C9SE01181A

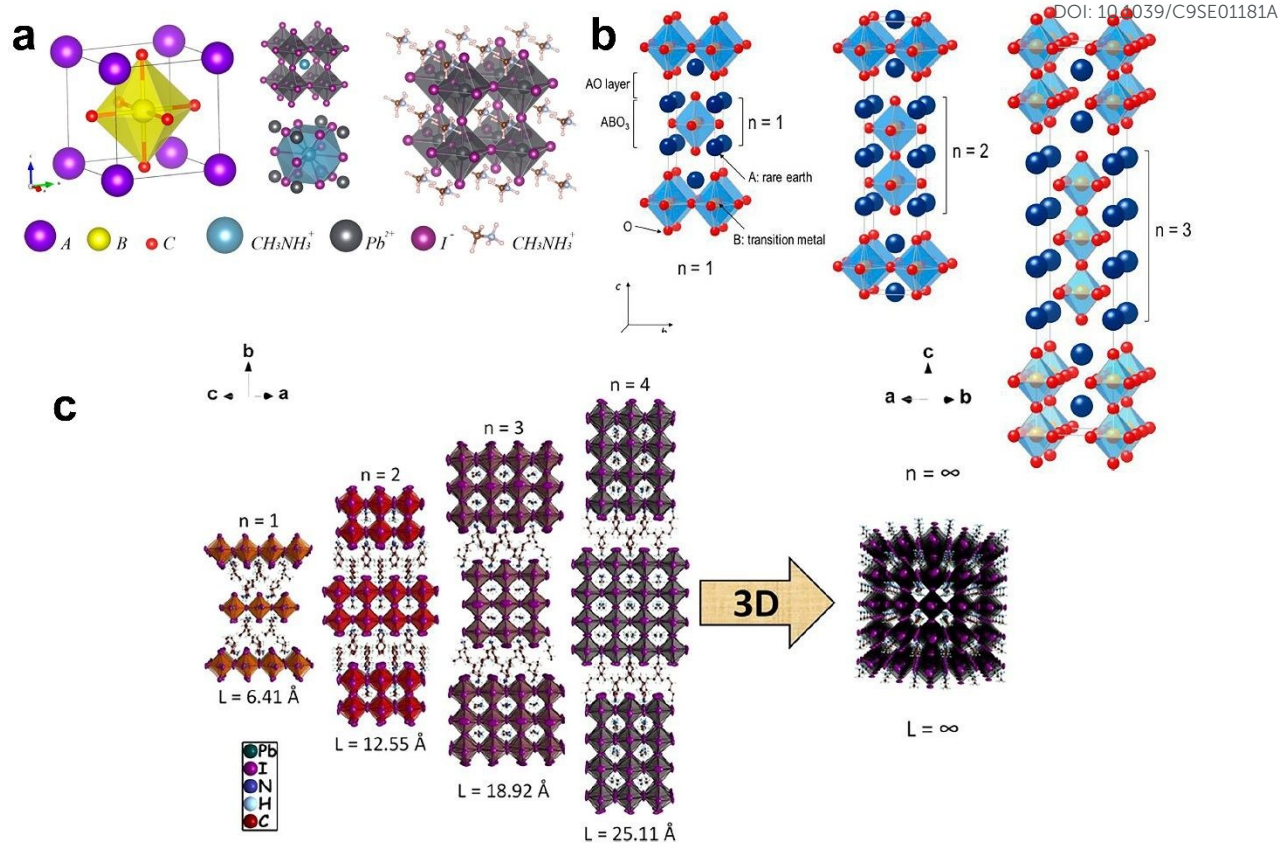

Fig. 1 (a) Unit cell of a general cubic perovskite and the coordination around the lead ions (octahedron) and the organic cations (cuboctahedron). Reproduced with permission from Ref.[75]. Copyright 2015, American Chemical Society. **(b)** Schematic crystal structures of all-inorganic members of Ruddlesden-Popper type $A_{n+1}B_nO_{3n+1}$ (n = 1, 2 and 3). The denotation of n represents the number of stacked octahedral layers separated by a rock-salt AO layer. Reproduced with permission from Ref.[80]. Copyright 2017, MDPI. **(c)** Crystal structures of the 2D lead iodide perovskites $(BA)_2(MA)_{n-1}Pb_nI_{3n+1}$ (n = 1 to ∞). The n-value denotes the thickness of the inorganic layer in each compound. The numerical values refer to the distance between the terminal iodide ions of each layer and are determined directly from the refined crystal structures. Reproduced with permission from Ref.[81]. Copyright 2016, American Chemical Society.

As well as the great development of 3D perovskites, organic–inorganic hybrid RP phases have also received much attention. The empirical formula of organic–inorganic hybrid RP phases can be written as $A_{n-1}A'_2B_nX_{3n+1}$, where A is a monovalent organic spacer; A' is a monovalent cation like $CH_3NH_3^+$, $CH(NH_2)_2^+$, or Cs^+; B is an octahedral coordinated covalent cation like Pb^{2+} or Sn^{2+}; and X is monovalent halogen anion like Cl^-, Br^-, or I^-. In Fig. 1c, a series of compounds, $(BA)_2(MA)_{n-1}Pb_nI_{3n+1}$ (BA = $CH_3(CH_2)_3NH_3^+$), is used as an example to illustrate the crystallographic structural features of organic–inorganic hybrid RP phases. Figure 1c shows that the organic–inorganic hybrid RP phases retain the structural features of the all-inorganic RP phases except that the long-chain organic spacer BA replaces the rock-salt layer of the all-inorganic phases. In Fig. 1c, 3D $MAPbI_3$ can be regarded as the parent prototype of the RP phases and for each 2D member, it can be viewed that the MA^+ are partially (n = 2, 3, 4, …) or fully (n =1) substituted by the terminal organic BA^+ cations. As the number of stacked octahedral layers n increases, the 2D character of the RP phase decreases and when n = ∞, which means there are no BA long-chain organic spacers, the parent prototype 3D perovskite $MAPbI_3$ will be obtained.

Compared with the 3D $MAPbI_3$ perovskite, unique structural features and properties emerge upon the introduction of organic spacers into RP phases. Layered perovskites are generally viewed as the periodic splitting of the 3D structure along a crystallographic plane, forming natural quantum well structures. When exposed to humidity, the 3D perovskite $MAPbI_3$ only remained stable for several days, whereas no evident changes were observed in RP phases under the same conditions.[67] The outstanding humidity resistance of RP phases can be ascribed to the organic spacers, which can prevent water molecules from penetrating into the crystallographic structure. In perovskites, the Pb–I octahedral layers can act as solar-cell absorbers. Thus, the coexistence of Pb–I layers and hydrophobic organic spacer layers in RP phases make this family promising candidates for use in solar cells. Apart from the important advantage of favorable hydrophobicity, RP phases usually exhibit better structural and thermal stabilities than those of 3D perovskites, which are also attributed to their unique crystallographic structures. The introduction of organic spacers also converts the enclosed construction of 3D perovskites to an open superlattice structure, which enables the crystal structure and material properties of RP perovskites to be readily tuned. By adjusting

View Article Online
DOI: 10.1039/C9SE01184A

the precursor stoichiometry in the material synthesis, continuous tuning of the dimensionality can be achieved. Thus, the layered RP perovskite structure may offer greater tunability at the molecular level for material optimization. One typical example of the property modulation of RP perovskites can be found in their band-gap tuning. For example, in the $(BA)_2(MA)_{n-1}Pb_nI_{3n+1}$ (n = 1– 4) series, the band gap decreases from 2.43 to 1.91 eV as n increases, and the band gap of $MAPbI_3$ (n = ∞) is only 1.48 eV (Table 2).[78, 81]

Table 2. Band gaps of $(BA)_2(MA)_{n-1}Pb_nI_{3n+1}$ perovskites.[78, 81]

Compound	Band gap E_g (eV)	Compound	Band gap E_g (eV)
$(BA)_2PbI_4$	2.43	$(BA)_2(MA)_2Pb_3I_{10}$	2.03
$(BA)_2(MA)Pb_2I_7$	2.17	$(BA)_2(MA)_3Pb_4I_{13}$	1.91
$MAPbI_3$	1.48		

Compared with 3D perovskites, the introduction of organic spacers into the crystal structure of RP perovskites does not yield only positive changes. As illustrated above, as the dimensionality decreases, the band gap widens, resulting in a deterioration in absorption performance in the visible region. The increase in band gap can be attributed to quantum and dielectric confinement effects, the latter of which not only widen the band gap but also confine electron–hole pairs and decrease the carrier mobility in layered RP phases.[69, 82] These two changes are undesirable for solar cell applications, which principally require strong light absorption overlapping with the solar spectrum and efficient separation of electron–hole pairs to produce a photocurrent.

3. Preparation methodology and enhanced stability

3.1 Preparation methodology

Various methods have been successfully adopted to synthesize RP perovskites. For applications of RP perovskites, such as highly efficient photodetectors, the micromorphology, phase purity, and thickness of the synthesized materials directly affect the final performance of the fabricated device. Therefore, in this section, recent progress in the synthesis of the RP perovskites is reviewed. The preparation of RP perovskites by four common approaches—solvent-based, colloidal-based, liquid- and gas-phase epitaxy, and exfoliation methods—are discussed. Additionally, progress of the single-crystal growth of RP perovskites is also presented in detail.

3.1.1 Solution-based synthesis. Solution-based methods represent a facile strategy to prepare 2D RP perovskites and are also fundamental for other subsequent controlled preparation methods, like mechanical exfoliation and thermal evaporation. Solution-based synthesis is currently the most widely used approach to prepare 2D RP perovskites.[68, 81, 83-88] To synthesize these materials, generally, covalent cation sources are first reacted with a halogen acid to produce a metal halide and the halogenated organic spacers are also prepared by reaction with the halogen acid. Then, the halogenated metal cations and organic spacers are mixed together in an appropriate ratio to produce the target material. To illustrate this process, the synthesis of the $(CH_3(CH_2)_3NH_3)_2(CH_3NH_3)_{n-1}Pb_nI_{3n+1}$ (n = 1–4) family is considered as an example.[68, 81] First, lead oxide (PbO) powder was dissolved in a mixture of aqueous HI solution and aqueous H_3PO_2 by heating to boiling under constant magnetic stirring for several minutes, resulting in the formation of a transparent bright yellow solution. An appropriate amount of CH_3NH_3I was then added into the hot reaction solution and stirred until the added solid was completely dissolved. Meanwhile, $CH_3(CH_2)_3NH_3I$ solution was prepared by slowly adding n-$CH_3(CH_2)_3NH_2$ dropwise into the stirred aqueous HI solution in an ice-water bath. After cooling to room temperature, the $CH_3(CH_2)_3NH_3I$ solution was poured into the hot solution containing dissolved PbO.

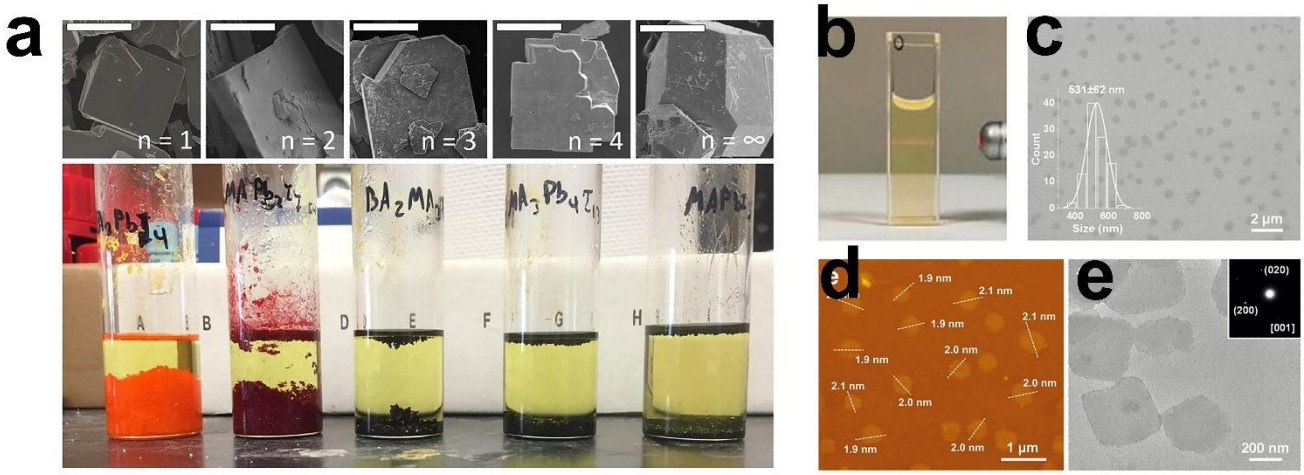

Fig. 2 (a) SEM images (top) and photographs of the $(BA)_2(MA)_{n-1}Pb_nI_{3n+1}$ perovskite crystals (bottom) (scale bars = 200 μm). Reproduced with permission from Ref. [81]. Copyright 2016, American Chemical Society. **(b)** Tyndall effect of $(PEA)_2PbI_4$ nanosheets in toluene. **(c)** SEM, **(d)** AFM, and **(e)** TEM images of single-layer $(PEA)_2PbI_4$ nanosheets. Insets: **(c)** Lateral size distribution of the as-synthesized $(PEA)_2PbI_4$ nanosheets and **(e)** SAED pattern of a typical $(PEA)_2PbI_4$ nanosheet. **(b)–(e)** Reproduced with permission from Ref. [89]. Copyright 2017, Wiley VCH.

View Article Online
DOI: 10.1039/C9SE01181A

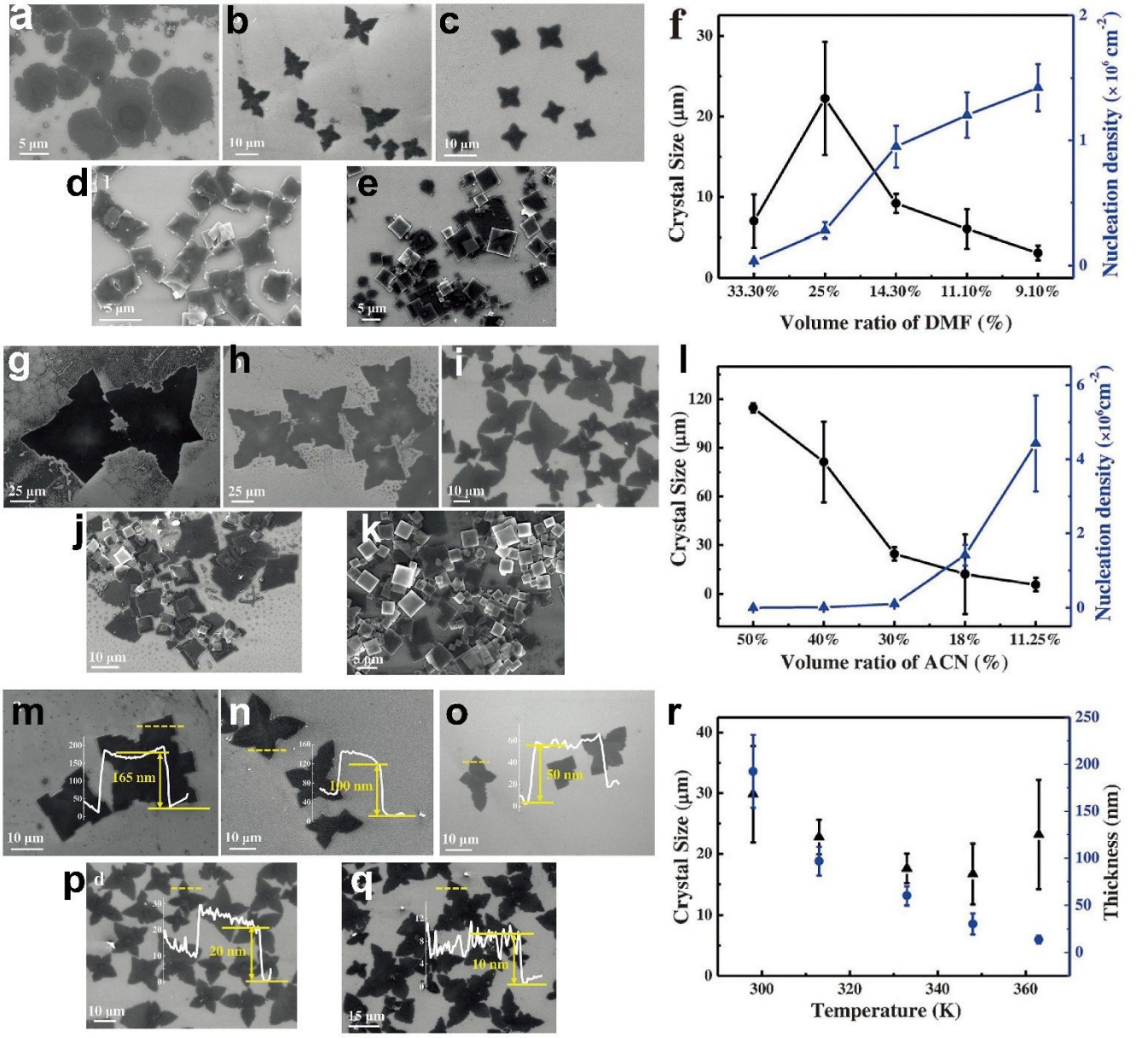

Fig. 3 Effects of the solvent volume ratio and crystallization temperature on perovskite morphology. SEM images illustrating the different morphologies of $(C_4H_9NH_3)_2PbBr_4$ perovskite grown using DMF ratios of **(a)** 33.3%, **(b)** 25%, **(c)** 14.3%, **(d)** 11.1%, and **(e)** 9.1%. **(f)** The size and nucleation density of $(C_4H_9NH_3)_2PbBr_4$ perovskite with respect to the DMF ratio. SEM images illustrating the different morphologies of $(C_4H_9NH_3)_2PbBr_4$ perovskite grown at ACN ratios of **(g)** 50%, **(h)** 40%, **(i)** 30%, **(j)** 18%, and **(k)** 11.25%. **(l)** Size and nucleation density of $(C_4H_9NH_3)_2PbBr_4$ perovskite with respect to the ACN ratio. SEM images of $(C_4H_9NH_3)_2PbBr_4$ perovskite grown at **(m)** 298 K, **(n)** 313 K, **(o)** 333 K, **(p)** 348 K, and **(q)** 363 K. Insets show corresponding AFM height profiles. **(r)** Temperature dependence of the thickness and size of $(C_4H_9NH_3)_2PbBr_4$ perovskite. **(a)–(r)** Reproduced with permission from Ref. [90]. Copyright 2017, Wiley VCH.

The reaction mixture was heated and stirred until no precipitate was observed. Then, the mixed solution was left to cool to room temperature, during which, deep-red or glossy black rectangular-shaped thin plates started to crystallize. By controlling the ratio of n-$CH_3(CH_2)_3NH_2$ to HI, the members with different *n* values in the $(CH_3(CH_2)_3NH_3)_2(CH_3NH_3)_{n-1}Pb_nI_{3n+1}$ series can be obtained, as shown in Fig. 2a. The precipitation was deemed to be complete after ~2 h. The crystals were isolated by suction filtration and then thoroughly dried under reduced pressure.[68] As described above, the organic spacer layers and perovskite-like layers are bound together by van der Waals interactions to afford a structure that affects nearly every property of the materials. In the synthesis of the $(CH_3(CH_2)_3NH_3)_2(CH_3NH_3)_{n-1}Pb_nI_{3n+1}$ (*n* = 1–4) family, the NH_3 groups in $CH_3(CH_2)_3NH_3I$ coordinate to the I^- ions in the PbI_4^{2-} network by forming hydrogen bonds to construct the 2D crystallographic structure.

Integrating a 2D RP perovskite prepared by a solution-based method into an optoelectronic device usually requires a

subsequent spin-coating process. An appropriate amount of the RP perovskite powder is dissolved in a selected solvent, for example, anhydrous dimethylformamide (DMF), under constant stirring to form a homogeneous solution. Thin films of the perovskite can then be deposited on a suitable substrate, like a silicon (Si) wafer, by spin coating the precursor solution under specific conditions. This approach is an extraordinary advantage of RP perovskites over $MAPbI_3$, because the poor crystallinity of $MAPbI_3$ leads to low surface coverage and large, non-uniform crystals, which are unfavorable for thin-film formation.

Although the solution-based synthesis of RP perovskites is quite straightforward and convenient, it usually results in inhomogeneous samples and undesired morphology, especially in the preparation of ultrathin samples. In other words, the precise control of the composition, phase purity, and morphology of RP perovskites is difficult using solution-based synthesis. To solve this problem, Chen et al.[90] systematically studied the synthesis of $(C_4H_9NH_3)_2PbBr_4$ from a chlorobenzene/DMF/acetonitrile (ACN) ternary solvent system. The effects of three critical factors including the solvent volume ratio, crystallization temperature, and solvent polarity on the growth dynamics of $(C_4H_9NH_3)_2PbBr_4$ were studied in detail. It was found that the precursor concentration and solvent polarity strongly influenced the morphology, including shape, lateral dimensions, and thickness, of the obtained perovskite samples. Figure 3 illustrates that when the precursor concentration was low (corresponding to high DMF and ACN concentrations), the $(C_4H_9NH_3)_2PbBr_4$ perovskite showed branched growth, suggesting a diffusion-controlled growth mechanism, and the obtained samples possessed star-like shapes. As the precursor concentration increased, the growth mode transformed into habit growth and regular cubic rather than the star-like samples. Sample thickness was directly related to both the crystallization temperature and solvent polarity. The polar groups of the solvent tended to adsorb on specific polar crystal planes and therefore hampered the self-assembly of the planes along the normal directions. Higher crystallization temperature also favored the formation of ultrathin films of the perovskite because the growth of the low-energy surfaces along the *c*-axis was greatly hindered at higher temperature. Within the scope of their study, the nucleation density increased monotonically with the precursor concentration, as shown in Fig. 3f and l.

3.1.2 Colloidal-based method. Generally, a RP perovskite precursor solution is prepared and then spin coated on a substrate like mesoporous TiO_2 or an Si wafer before solvent evaporation. The resulting samples usually crystallize into different lateral dimensions and thickness, which greatly limits further applications of the RP perovskite films. In 2017, Yang and co-workers found that the colloidal-based method provided an alternative way to synthesize ultrathin 2D RP perovskites in a more controllable and facile manner than the solution-based approach.[89] The procedures used in the colloidal-based method are quite similar to those used in the solvent-based one. However, the pre-synthesized perovskite precursor solution is dropped into toluene under vigorous stirring in the colloidal-based method instead of being dropped onto a substrate. A typical Tyndall effect was clearly observed after 10 min of stirring the toluene-based mixture, indicating the colloidal nature of the product, as shown in Fig. 2b. Using the colloidal-based method, single- and few-layer $(PEA)_2PbI_4$ nanosheets with lateral dimensions of 531±62 nm and thickness of 2.0±0.1 nm were successfully obtained (Fig. 2c–e). By using different perovskite precursors, this method can also be extended to the synthesis of other single- or few-layer 2D RP phases with different compositions, like $(PEA)_2PbBrI_3$, $(PEA)_2PbBr_4$, and $(PEA)_2PbCl_4$. By replacing toluene with other polar solvents, such as chlorobenzene, chloroform, or dichloromethane, the lateral dimensions of the samples can be finely tuned.

3.1.3 Liquid- and vapor-phase epitaxy method. Single-crystalline flakes with few layers and low defect density can be obtained by careful selection of the solvent and precise control of the precursor composition and evaporation conditions in the solution-based method or exfoliation from well-developed bulk single crystals. Although such high-quality flakes can provide opportunities for intrinsic property evaluation, the additional transfer process needed to fabricate semiconductor devices limits the compatibility of the flakes with substrates. This problem is avoided in the case of the epitaxy method because mature solutions have already been developed in the semiconductor industry. Thus, the epitaxy method can provide potential solutions to integrate 2D RP phases into optoelectronic devices.[91-94] Considering these advantages, the epitaxy method was quickly implemented in the growth of 3D perovskites and then extended to the preparation of 2D RP perovskites.[95-106] As early as 1997, a dual vapor deposition source of lead iodide and organic ammonium iodide was used to prepare $(RNH_3)_2PbI_4$ films, although the resulting films were defect-rich and disordered.[107] Recently, single-crystalline $(C_4H_9NH_3)_2PbI_4$ flakes with smooth surfaces and high optical quality were successfully prepared by vapor-phase deposition through careful optimization of the deposition conditions.[97] By employing mica as the substrate and taking advantage of the weak van der Waals interactions between the substrate and 2D RP phases, single-crystalline flakes with regular orientation along both epitaxial directions were obtained (Fig. 4a). These flakes possessed lateral dimensions of 5–10 μm and thicknesses of less than 80 nm (Fig. 4b). Moreover, their root-mean-square roughness was as low as 0.55 nm in the highlighted region in Fig. 4c, revealing their excellent surface smoothness. Using this van der Waals epitaxy method, flakes of $(C_4H_9NH_3)_2PbI_4$ with well-controlled dimensions and different thickness were successfully obtained on both mica and Si substrates.[101] As shown in Fig. 4d and e, over 90% of the flakes were oriented parallel indicating epitaxy has been obtained. In addition, step structures were observed, which means that the growth of $(C_4H_9NH_3)_2PbI_4$ followed the 2D layer-by-layer mechanism. Vapor-phase epitaxy also plays an important role in the fabrication of heterostructures. In 2017, a general low-temperature synthetic strategy was developed to synthesize $(n\text{-}C_4H_9NH_3)_2PbI_4/(n\text{-}C_4H_9NH_3)_2MAPb_2I_7$ heterostructures.[99] This strategy consists of two independent

View Article Online
DOI: 10.1039/C9SE01181A

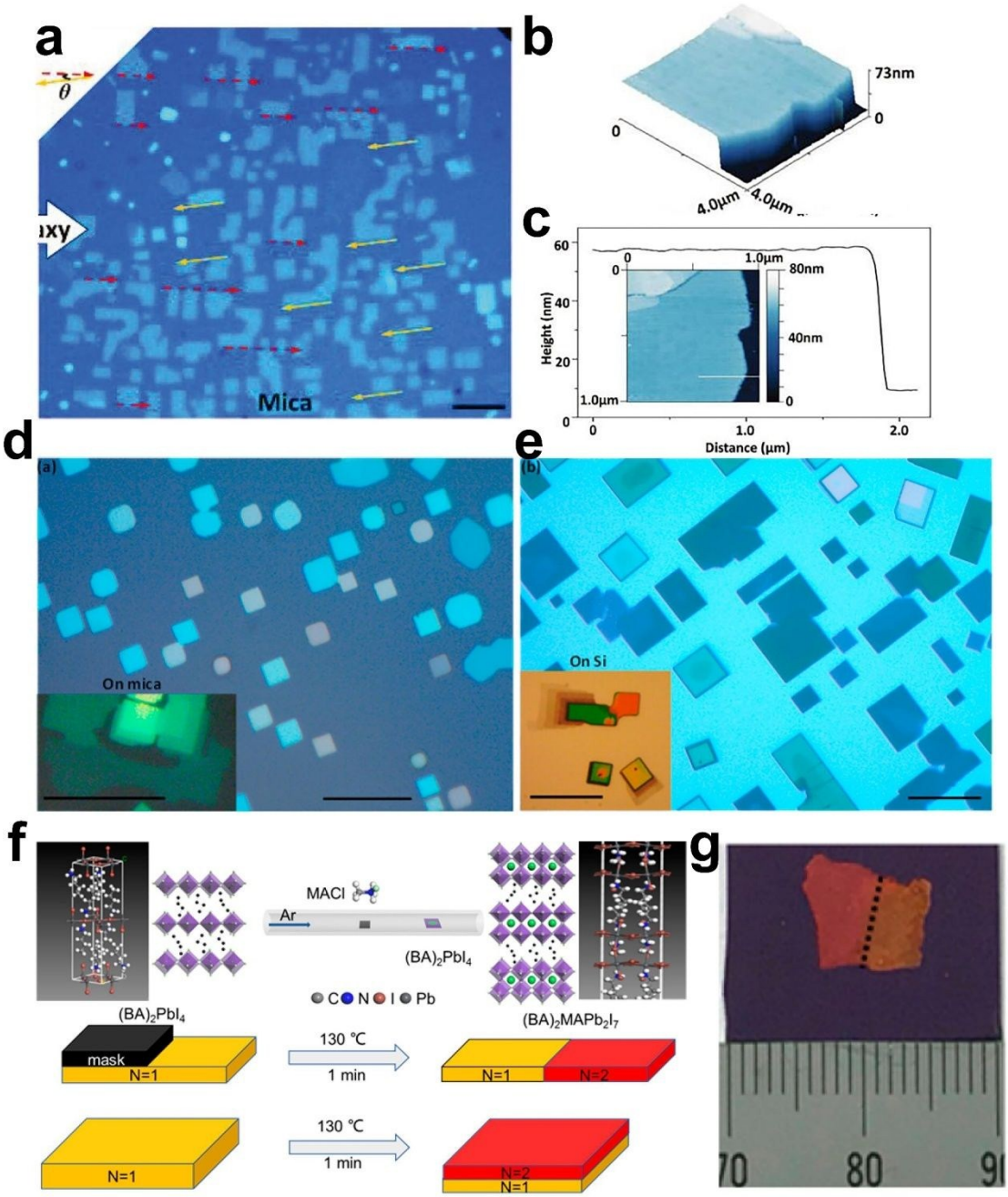

Fig. 4 Vapor epitaxy method for the synthesis of Ruddlesden–Popper perovskites. **(a)** Epitaxial $(C_4H_9NH_3)_2PbI_4$ flakes formed on mica by co-evaporation. **(b)** Height profile of a $(C_4H_9NH_3)_2PbI_4$ flake. **(c)** Height line scan of a $(C_4H_9NH_3)_2PbI_4$ flake, exhibiting excellent surface smoothness. **(a)–(c)** Reproduced with permission from Ref. [97]. Copyright 2017, Wiley VCH. **(d, e)** $(C_4H_9NH_3)_2PbI_4$ flakes grown on muscovite mica and Si (001), respectively, through the van der Waals epitaxy method. The edges of most rectangular flakes were parallel, indicating that epitaxy was obtained. The insets are enlarged images of the epitaxial flakes, in which step structures were observed, indicating a 2D layer-by-layer growth mechanism. Scale bars represent 20 μm. **(d, e)** Reproduced with permission from Ref. [101]. Copyright 2018, American Chemical Society. **(f)** Schematic illustrations of the crystal structural evolution from $(C_4H_9NH_3)_2PbI_4$ to $(C_4H_9NH_3)_2MAPb_2I_7$ and the corresponding gas–solid phase intercalation process for the preparation of lateral and vertical $(C_4H_9NH_3)_2PbI_4/(C_4H_9NH_3)_2MAPb_2I_7$ heterostructures. **(g)** Photograph of a lateral $(C_4H_9NH_3)_2PbI_4/(C_4H_9NH_3)_2MAPb_2I_7$ heterostructure. The distinct color contrast indicates the formation of the heterostructure. Reproduced with permission from Ref. [99]. Copyright 2017, American Chemical Society.

procedures, as shown in Fig. 4f. First, flakes of (n-$C_4H_9NH_3)_2PbI_4$ were grown using the traditional solution-based method, as discussed above in Section 3.1.1. A gas–solid-phase intercalation process was then used to convert part of the as-grown (n-$C_4H_9NH_3)_2PbI_4$ to (n-$C_4H_9NH_3)_2MAPb_2I_7$ and form a heterostructure. In this procedure, the conversion of (n-$C_4H_9NH_3)_2PbI_4$ was realized by placing the as-grown flakes in MAI or MACl vapor using high-purity Ar as a carrier gas. During this procedure, synergistic rearrangements of the halide and n-butylamine ions are needed for the intercalation of the small MA cations into the center of PbI_6 octahedra. Depending on whether or not a mask was used, both lateral and vertical

View Article Online
DOI: 10.1039/C9SE01181A

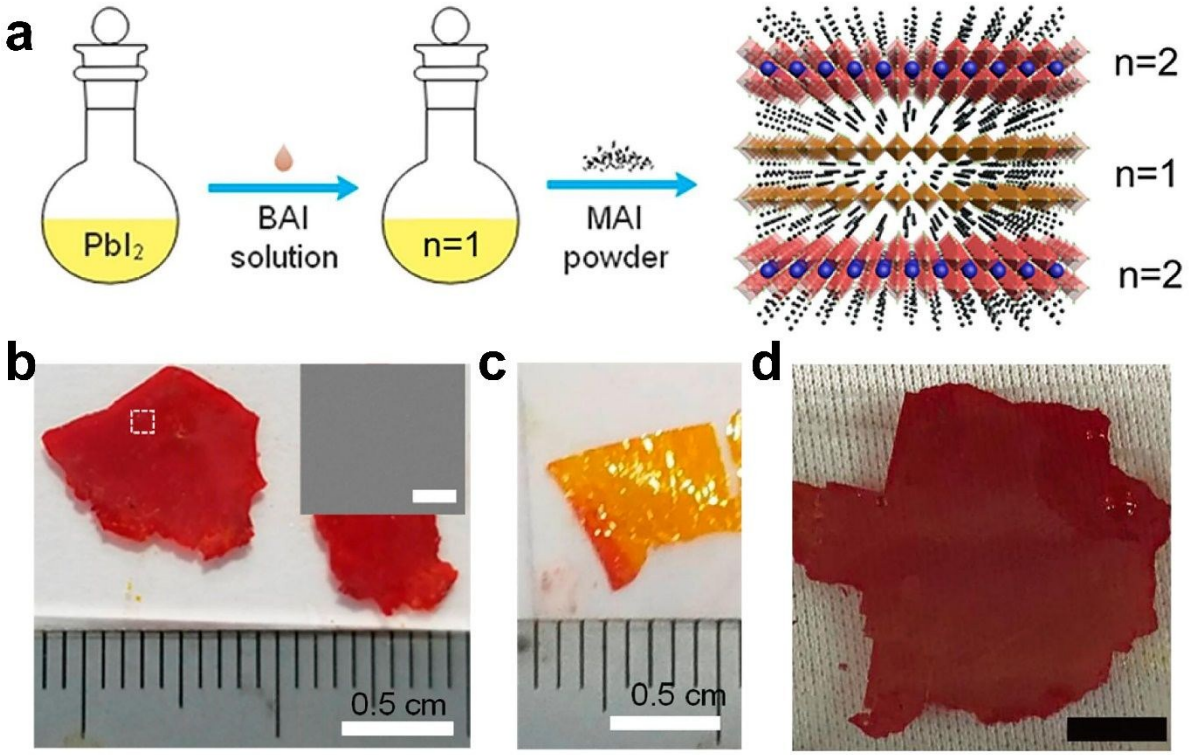

Fig. 5 Liquid-phase epitaxy method for the synthesis of Ruddlesden–Popper perovskites. **(a)** Schematic illustration of the solution-based synthetic process and the crystal structure of the $(C_4H_9NH_3)_2PbI_4/(C_4H_9NH_3)_2MAPb_2I_7$ heterostructure. **(b)** Photograph of the $(C_4H_9NH_3)_2PbI_4/(C_4H_9NH_3)_2MAPb_2I_7$ heterostructure produced using a growth time of 240 min. **(c)** Photograph of the exfoliated plates. The distinct color contrast of the plate indicates the formation of a heterostructure. **(a)–(c)** Reproduced with permission from Ref. [105]. Copyright 2019, American Chemical Society. **(d)** Photograph of the $(C_4H_9NH_3)_2PbI_4/(C_4H_9NH_3)_2MAPb_2I_7$ heterostructure grown by the solution epitaxy method. The scale bar represents 0.5 cm. Reproduced with permission from Ref. [106]. Copyright 2019, Wiley VCH.

heterostructures, respectively, were successfully obtained. Figure 4g shows a photograph of the lateral $(C_4H_9NH_3)_2PbI_4/(C_4H_9NH_3)_2MAPb_2I_7$ heterostructure. The distinct color contrast indicates the formation of the heterostructure.

Apart from the vapor-phase epitaxy, the liquid-based epitaxy method has also been employed in the synthesis of RP perovskites. In 2019, Li and colleagues developed a solution-based method for the facile synthesis of centimeter-sized $(C_4H_9NH_3)_2PbI_4/(C_4H_9NH_3)_2(CH_3NH_3)Pb_2I_7$ heterostructures.[105, 106] As shown in Fig. 5a, they carefully adjusted the reaction sequence of the precursors as follows: a butylamine iodide (BAI) solution was first injected into a bright yellow PbI_2 solution at 80 °C, followed by addition of MAI powder rather than in the opposite sequence. Taking advantage of the increasing solubility of the RP perovskite series with *n*, during the cooling process, flakes of the *n* = 1 RP perovskite $(C_4H_9NH_3)_2PbI_4$ started to precipitate from the solution first because of its low solubility. After the temperature was lowered to 75 °C, subsequent slight drops in temperature led to the crystallization of $(C_4H_9NH_3)_2MAPb_2I_7$ onto the as-grown *n* = 1 perovskite flakes through the intercalation of MA cations into the center of PbI_6^{4-} octahedra of the *n* = 1 perovskite while BAI molecules were released into the solution to maintain the 2D layered structure. Through fine adjustment of the reaction sequence and cooling rate, centimeter-sized heterostructures with high quality and purity were obtained. In Fig. 5a and c, the exterior of the flakes consisting of *n* = 2 $(C_4H_9NH_3)_2MAPb_2I_7$ is red, while the interior consisting of the *n* = 1 $(C_4H_9NH_3)_2PbI_4$ is yellow. This distinct color contrast clearly reveals the formation of the $(C_4H_9NH_3)_2PbI_4/(C_4H_9NH_3)_2MAPb_2I_7$ heterostructure.

At present, although the controllable, scalable, and stable preparation of large-sized 2D RP perovskite films and heterostructures still remains challenging, there is every reason to expect that the epitaxy method will yield further intriguing results in the future.

3.1.4 Exfoliation method. It is well known that when the dimensions of a material decrease to a certain degree, unique characteristics different from those of the bulk material emerges. For this reason, ultrathin sheets that are just one unit cell thick are required. The 2D structural characteristics of RP phases with strong van der Waals interactions make the preparation of thin films quite straightforward and the formation of their bulk samples difficult, especially for those with lower *n* values. Because of this structural feature, the exfoliation method has been widely used to fabricate ultrathin films of 2D perovskites since their initial development and numerous achievements have been made.[108-114] According to

View Article Online
DOI: 10.1039/C9SE01181A

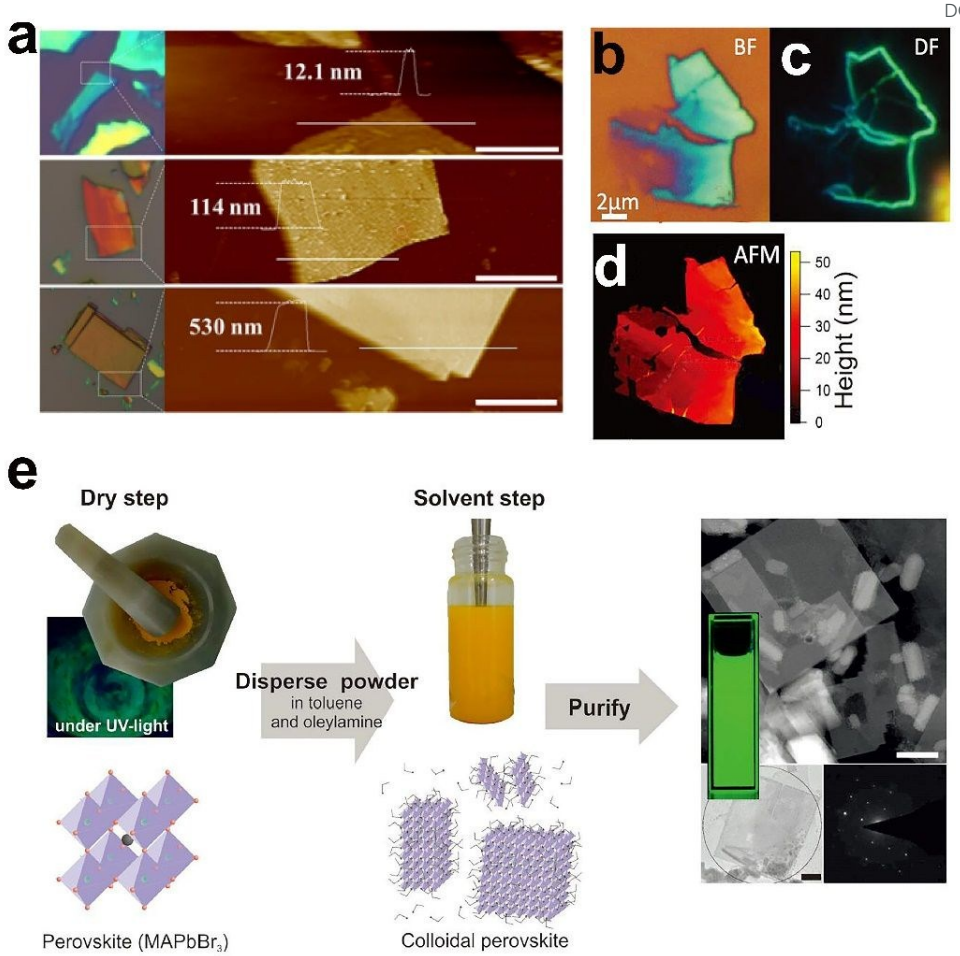

Fig. 6 The exfoliation method for the synthesis of 2D RP phases. **(a)** Optical and AFM images of exfoliated n = 3 2D perovskite microplates with different thicknesses. Scale bars from top to bottom represent 2, 4, and 10 μm. Reproduced with permission from Ref. [113]. Copyright 2018, IOP Publishing, Ltd. Images at 100× magnification using **(b)** bright and **(c)** dark fields of an exfoliated hexagonal $(C_6H_9C_2H_4NH_3)_2PbI_4$ flake. **(d)** AFM image of the same area. **(b)–(d)** Reproduced with permission from Ref. [108]. Copyright 2014, AIP Publishing. **(e)** Schematic of the synthesis of perovskite nanocrystals. A powder of methylammonium halide (MAX) and PbX_2 was ground with a pestle and mortar. Perovskite formation was monitored by the color change of the powder. The perovskite powder was dispersed in toluene with oleylamine and tip-sonicated for 30 min, after which the dispersion was purified to obtain highly fluorescent perovskite nanocrystals. The resulting crystals were polydisperse in size and shape, but showed extremely high crystallinity. Reproduced with permission from Ref. [112]. Copyright 2016, Wiley VCH.

the nature of the process, exfoliation methods can be divided into mechanical exfoliation and chemical exfoliation, the former of which has been widely used to prepare ultrathin sheets. In 2018, Li et al.[113] creatively employed the mechanical exfoliation method to fabricate $(C_4H_9NH_3)_2(CH_3NH_3)_{n-1}Pb_nI_{3n+1}$ (n>2) microplates with pure single n perovskites (Fig. 6a) and successfully integrated the exfoliated single n RP microplates with 2D hexagonal boron nitride (hBN) flakes to construct a two-probe photodetector, which could advance the design of functional optoelectronic devices. Using a micromechanical exfoliation method, Niu and co-workers obtained mono-and few-layer $(C_6H_9C_2H_4NH_3)_2PbI_4$ flakes.[108] Their measurement results demonstrated a clear difference in the exciton properties between "bulk" (>15 layers) and very thin (<8 layers) regions (Fig. 6b–d) caused by the structural rearrangement of organic molecules around the inorganic sheets.

In addition to mechanical exfoliation, ligand-assisted liquid-phase exfoliation has also been used to lower the dimensions of bulk $MAPbX_3$ (X = I^-, Br^-, Cl^-, or mixed halide ions) prepared by the solid-state method from a specific thickness down to a single perovskite layer.[112] As shown in Fig. 6e, $CH_3NH_3PbBr_3$ was synthesized by grinding CH_3NH_3Br and $PbBr_2$ together. The perovskite powder was then dispersed in toluene together with oleylamine (OlA) and subjected to tip sonication. By careful optimization of the sonication conditions, perovskite plates with extremely high crystallinity were obtained. In this case, toluene and OlA were used as solvents. The experimental results indicated that the OlA ligand assisted in the exfoliation, protected the obtained nanocrystals from agglomeration, and rendered them dispersible in organic solvents.

3.1.5 Single-crystal growth. Although various synthesis methods have already been developed to prepare 2D RP phases, there are few reports of the growth of bulk single-crystal materials. However, bulk single crystals of high quality

View Article Online
DOI: 10.1039/C9SE01181A

are critical for both fundamental studies and efficient devices (especially photodetectors) because the performance of

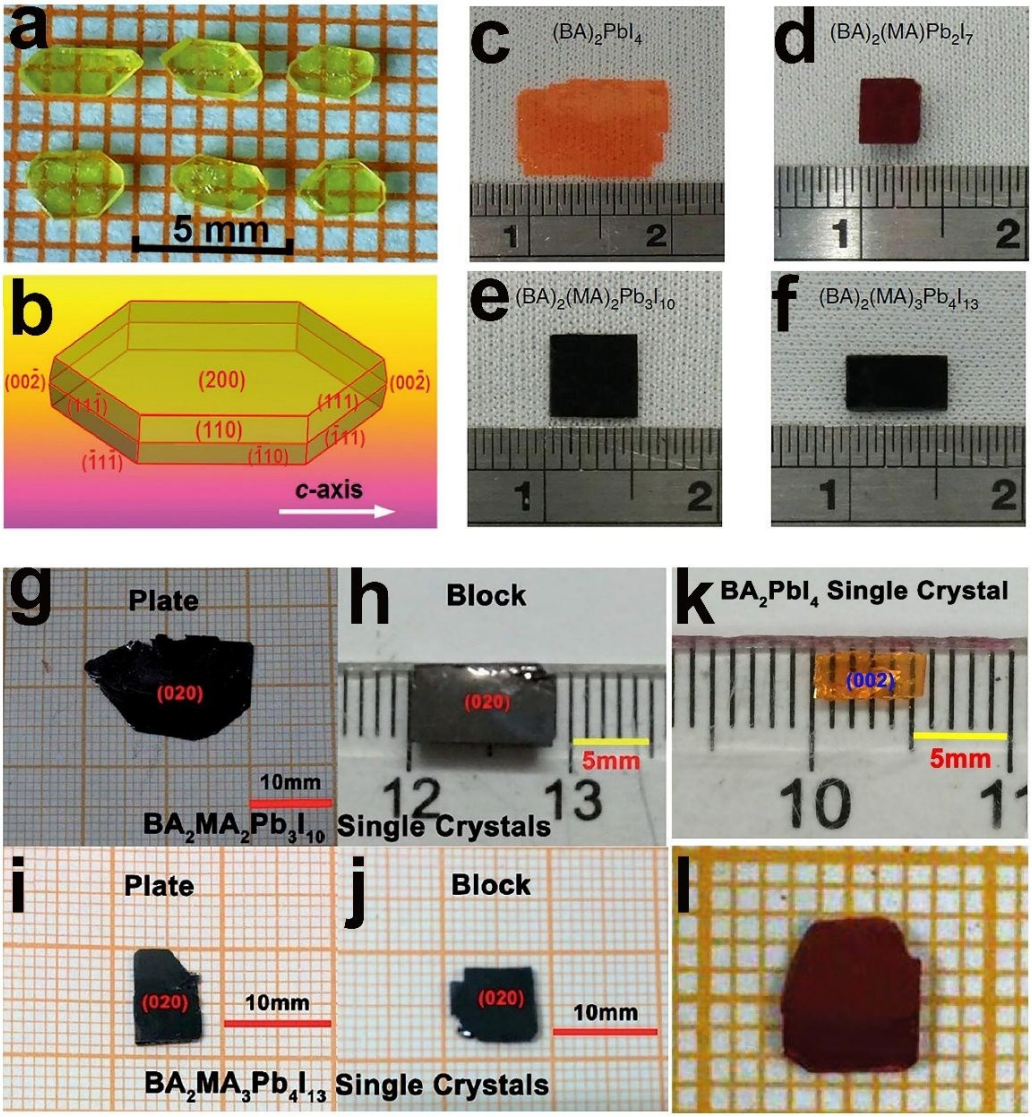

Fig. 7 Single crystals of RP phases grown by the temperature-cooling method. **(a)** Block crystals of $(C_4H_9NH_3)_2(CH_3NH_3)_2Pb_3Br_{10}$ and **(b)** the typical growth morphology of the crystals. **(a)**, **(b)** Reproduced with permission from Ref. [115]. Copyright 2017, Wiley VCH. **(c)–(f)** Photographs of centimeter-sized RP single crystals with n = 1–4 in the $(CH_3(CH_2)_3NH_3)_2(CH_3NH_3)_{n-1}Pb_nI_{3n+1}$ series. **(c)–(f)** Reproduced with permission from Ref. [116]. Copyright 2018, Springer Nature. **(g)–(j)** Photographs of plate- and block-shaped single crystals of $BA_2MA_2Pb_3I_{10}$ (**(g)** and **(h)**) and $BA_2MA_3Pb_4I_{13}$ (**(i)** and **(j)**) obtained by the TSSG method. **(k)** A BA_2PbI_4 single crystal grown by the TSSG method. **(g)–(k)** Reproduced with permission from Ref. [117]. Copyright 2018, RSC Publishing. **(l)** Photograph of a $(PA)_2(G)Pb_2I_7$ bulk single crystal with dimensions of 5.5×4.2×0.9 mm. Reproduced with permission from Ref. [118]. Copyright 2019, Wiley VCH.

polycrystalline samples is usually limited by the boundary-induced low chemical durability[119], poor uniformity, high defect density[25], and short carrier diffusion length[33]. Furthermore, the lack of well-developed bulk single crystals also hampers the full characterization of the anisotropic properties of RP perovskites and thus hinders further insights into their property–structure relationships. The highly anisotropic properties of 2D RP perovskites caused by their natural quantum well structures are of great interest. The study of single-crystal growth also favors the deeper understanding of the growth mechanism of RP perovskites and feeds back to the design of novel preparation methods. Therefore, recent progress of the bulk single-crystal growth of RP perovskites is summarized in this section.

View Article Online
DOI: 10.1039/C9SE01181A

ARTICLE

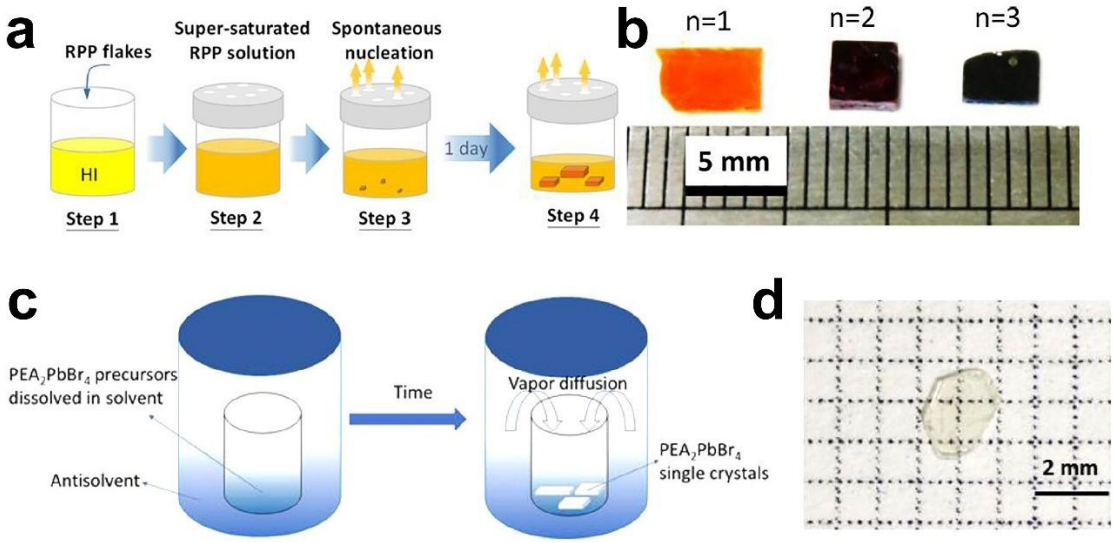

Fig. 8 (a) Growth process of homologous 2D RP single crystals by slow evaporation using a constant-temperature solution growth strategy. **(b)** As-grown crystals of $(BA)_2(MA)_{n-1}Pb_nI_{3n+1}$ (n = 1–3). **(a)**, **(b)** Reproduced with permission from Ref. [120]. Copyright 2018, American Chemical Society. **(c)** Schematic diagram of the growth process of 2D $(PEA)_2PbBr_4$ perovskite single crystals. **(d)** Photograph of a transparent 2-mm $(PEA)_2PbBr_4$ single crystal. **(c)**, **(d)** Reproduced with permission from Ref. [121]. Copyright 2017, American Chemical Society.

View Article Online
DOI: 10.1039/C9SE01181A

ARTICLE

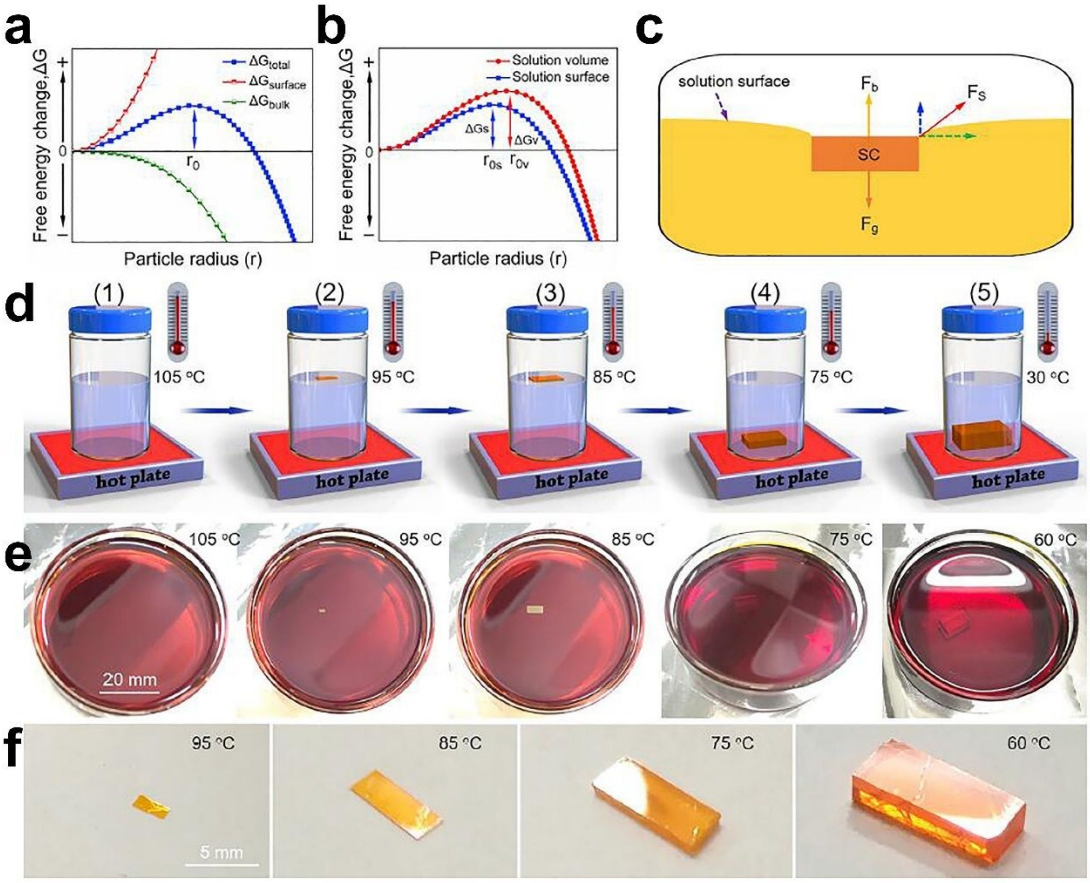

Fig. 9 Crystallization of $(PEA)_2PbI_4$ 2D RP perovskite single crystals. **(a)** Gibbs free energy change ΔG_{total} as a function of particle radius. ΔG_{total} consists of a surface term ΔG_s and a bulk term ΔG_b. **(b)** Graph illustrating the lower nucleation barrier for the solution surface compared with that in the solution volume. **(c)** Schematic of a single crystal staying afloat on a solution surface. **(d)** Schematic of the surface tension-controlled crystallization process. **(e)** Photographs of $(PEA)_2PbI_4$ single crystals grown at different temperatures. **(f)** Corresponding photographs of $(PEA)_2PbI_4$ single crystals obtained at different temperatures. Reproduced with permission from Ref. [122]. Copyright 2019, Elsevier.

When the solubility of the target crystals in the corresponding acid halide solvents is moderate and changes considerably with the temperature in a suitable range, the temperature-lowering method can be used as an efficient and simple way to grow crystals. In this approach, a decrease of the temperature induces supersaturation of the growth solution, causing the target material to crystallize spontaneously or attach to an existing seed crystal, which is also called the top-seeded solution growth (TSSG) method or bottom-seeded solution growth (BSSG) method according to the position where the seed crystal are fixed. The temperature-lowering method has been widely used for the growth of 3D perovskite crystals[21, 22, 78, 123-126] and has also been extended to the growth of 2D RP perovskite crystals. As seen in Fig. 7, some well-developed bulk single crystals of RP perovskites have been obtained through this method. Generally, the as-grown single crystals exhibit a plate growth habit because of the layered crystallographic structure of RP perovskites. The macromorphology of the crystals coincides well with the theoretical one (Fig. 7a and b) because of the few restrictions on the crystals grown by this method. Overall, the temperature-lowering method provides a simple, convenient, and efficient path for the growth of RP perovskite crystals and the obtained crystals are usually of high quality. However, crystal growth using this method is always time-consuming (several days to months) and the exploration and optimization procedures to determine an appropriate solvent system are usually difficult.

Apart from lowering temperature, there are some other ways to make a growth solution supersaturated; for example,

solvent evaporation or the introduction of an antisolvent. As shown in Fig. 8a and b, slow evaporation of a constant-temperature solution was used to grow the RP perovskites $(BA)_2(MA)_{n-1}Pb_nI_{3n+1}$ (n = 1–3).[120] The schematic illustration in Fig. 8a displays the step-by-step process of crystal growth. Using this process, more efficient control of the rapid nucleation and decreased multicrystalline stacking of 2D perovskite flakes were successfully realized compared with the case for the temperature-cooling method. As shown in Fig. 8b, well-shaped millimeter-scale single crystals with high phase purity were obtained by using the solvent evaporation method. Figure 8c presents a schematic illustration of the modified antisolvent evaporation-assisted crystallization used to grow RP perovskite $(PEA)_2PbBr_4$ crystals.[121] By controlling the diffusion rate of the antisolvent (DMF and chlorobenzene in this case) vapor, transparent millimeter-sized 2D RP perovskite $(PEA)_2PbBr_4$ single crystals of high quality and phase purity were successfully grown (Fig. 8d).

As illustrated previously, 2D RP perovskites are expected to display highly anisotropic properties because of their natural quantum well structures and therefore bulk single crystals are imperative for the full characterization of the intrinsic properties of these materials, especially their anisotropic carrier transport properties. Although several growth methods have already been proposed, as discussed above, and millimeter-sized single crystals have been successfully obtained, their dimensions were all not sufficiently large to allow the full comprehension of their anisotropic carrier transport properties.[127-129] Recently, bulk high-quality single crystals of $(PEA)_2PbI_4$ with dimensions as large as 36 mm were grown through a surface tension-controlled crystallization method.[122] As shown in Fig. 9a, the classical nucleation theory indicates that only when the solution is sufficiently supersaturated can the energy fluctuation compensate for the nucleation energy barrier and nuclei with radii larger than the critical value, r_0, stably form and grow into large crystals. However, further study revealed that the critical nucleation barrier at the solution surface is lower than that in the solution. Thus, as illustrated in Fig. 9b, the nucleation probability at the surface layer is expected to be higher than that in the solution. Initially, the small crystallites are not large enough to overcome the synthetic effect of the surface tension (F_s) and buoyant force (F_b) (Fig. 9c). As a result, small crystallites can be held on the solution surface until they grow large enough to overcome F_b. Based on this analysis, a surface tension-controlled crystallization method was carefully designed, as schematically illustrated in Fig. 9d. Photographs of the $(PEA)_2PbI_4$ single crystals at each temperature-cooling stage are shown in Fig. 9e and f. Finally, high-quality bulk single crystals as large as 36 mm were obtained, which greatly favors the further study of the anisotropic properties of RP perovskites.

Advanced optoelectronic devices usually require large-area single-crystal films. However, an exfoliation process is necessary for single crystals grown by the temperature-cooling, solvent evaporation, and surface tension-controlled crystallization methods, which inevitably induces structural damage because of the weak van der Waals interactions in RP perovskites. Therefore, it is desirable to obtain free-standing 2D RP perovskite single crystals without an exfoliation process to facilitate the development of integrated advanced optoelectronic devices. With this goal in mind, a rapid synthetic route to free-standing 2D perovskite single crystals was designed and membranes of $(C_4H_9NH_3)_2(CH_3NH_3)_{n-1}Pb_nI_{3n+1}$ (n = 1–4 and ∞) were successfully obtained at a water–air interface.[130] By taking advantage of the differences between the ammonium heads and alkyl groups as shown in Fig. 10a–d, the alkylammonium cations $C_4H_9NH_4^+$ aligned in a "head-down" manner at a water–air interface, acting as a soft template to guide the nucleation and subsequent growth of RP perovskite crystals. Theoretical analysis revealed that this system had a lower nucleation energy and higher growth rate at the water–air interface compared with those in the out-of-plane directions, which led to film-like growth. Snapshots of the lateral growth of the 2D (n = 1), quasi-2D (n = 2), and 3D (n = ∞) members of the $(C_4H_9NH_3)_2(CH_3NH_3)_{n-1}Pb_nI_{3n+1}$ series are shown in Fig 10e, f, and g, respectively. Inch-size free-standing quasi-2D RP perovskite single crystal membranes with an aspect ratio as large as 10^4 were grown by this method, helping to bridge the gap between single-crystal devices and emerging quasi-2D perovskite materials.

View Article Online
DOI: 10.1039/C9SE01181A

ARTICLE

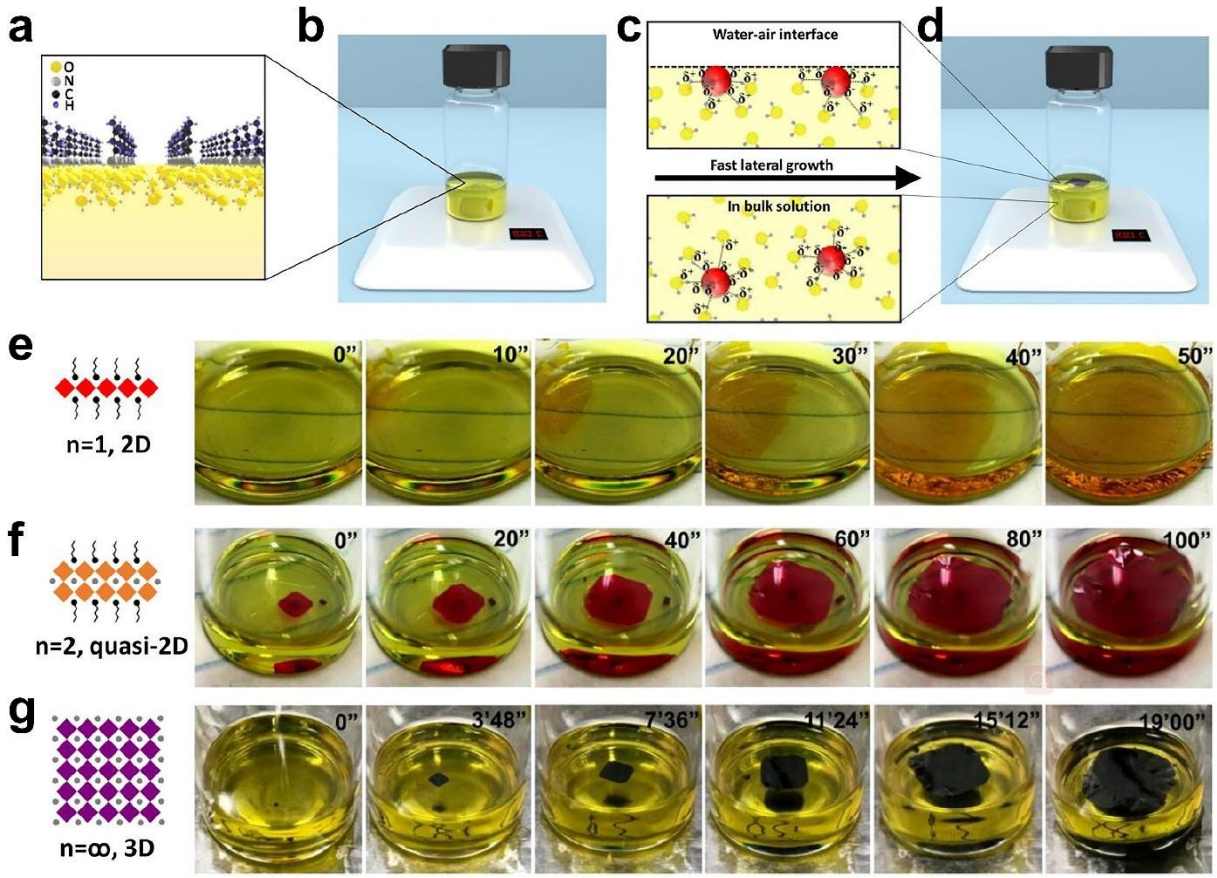

Fig. 10 Crystallization of quasi-2D $(C_4H_9NH_3)_2(CH_3NH_3)_{n-1}Pb_nI_{3n+1}$ perovskite single-crystal membranes. **(a)** Schematic illustration of the alignment of the butylammonium cation surfactant at the water–air interface to template nucleation. **(b)** Experimental setup during nucleation. **(c)** Molecular interaction between precursor molecules (red) and water molecules (yellow). Lower interaction energy is expected for the surface-layer molecules than those in bulk solution because of surface tension. **(d)** Experimental setup during crystal growth. Snapshots of the fast lateral growth of **(e)** 2D (n = 1), **(f)** quasi-2D (n = 2), and **(g)** 3D (n = ∞) single-crystal membranes. Reproduced with permission from Ref. [130]. Copyright 2018, American Chemical Society.

3.2 Enhanced stability

Although the 3D perovskites like $MAPbI_3$ exhibit fascinating properties and are important in various devices such as highly efficient photodetectors, solar cells, and light-emitting diodes, their poor stability in the ambient environment greatly hampers their practical application. A major reason that 2D RP phases have drawn intense research consideration is their superior long-term stability over that of 3D perovskites. In this section, recent progress in the stability enhancement of 2D RP perovskite materials is reviewed.

Generally, smaller molecules are more sensitive to ambient moisture than larger ones and the material structure tends to disintegrate after long-term exposure to moisture. In 3D perovskites, the monovalent cations are all small molecules with single carbon atoms, like MA^+ and FA^+, because the 3D perovskite structures are thermodynamically unstable when larger molecules are located within the PbI_2 framework. However, there are no such problems in RP phases because their open architecture allows the intercalation of long-chain alkylamine or large aromatic amines that act as organic spacers. The organic spacers can behave as insulating layers to protect the PbI_2 framework from the invasion of humidity. For example, films of $MAPbI_3$ and $(BA)_2(MA)_{n-1}Pb_nI_{3n+1}$ (n = 1–4) RP perovskites were prepared by spin coating and then their ambient stability under the same conditions was studied.[68] Figure 11a shows that the film of $(BA)_2(MA)_2Pb_3I_{10}$ remained unchanged after 2 months of exposure to 40% humidity with no additional PbI_2 diffraction peaks observed in its X-ray diffraction (XRD) patterns. In addition, no evident degradation was witnessed for the $(BA)_2(MA)_{n-1}Pb_nI_{3n+1}$ (n = 1, 2, and 4) films, as illustrated in Fig. 11b. In contrast, the film of $MAPbI_3$

gradually decomposed to yellow PbI_2 after a short time in the humid atmosphere because of the gradual loss of MA^+ (Fig. 11b). The moisture resistance of the 2D perovskites may be attributed to the hydrophobicity of the long BA cation chain and the highly oriented and dense nature of the perovskite films, which prevent direct contact of adventitious water with the perovskite.[68] Based on this point of view, Zheng et al.[66] systematically studied the stability of four quasi-2D perovskites $(C_6H_5CH_2NH_3)_2(FA)_8Pb_9I_{28}$ ($(BE)_2(FA)_8Pb_9I_{28}$), $((CH_3)_2NH_2)_2(FA)_8Pb_9I_{28}$ ($(DI)_2(FA)_8Pb_9I_{28}$), $((CH_2)_3(NH_3)_2)(FA)_8Pb_9I_{28}$ ($(PR)(FA)_8Pb_9I_{28}$), and $((CH_2)_4(NH_3)_2)(FA)_8Pb_9I_{28}$ ($(BU)(FA)_8Pb_9I_{28}$) under humid conditions. The humidity

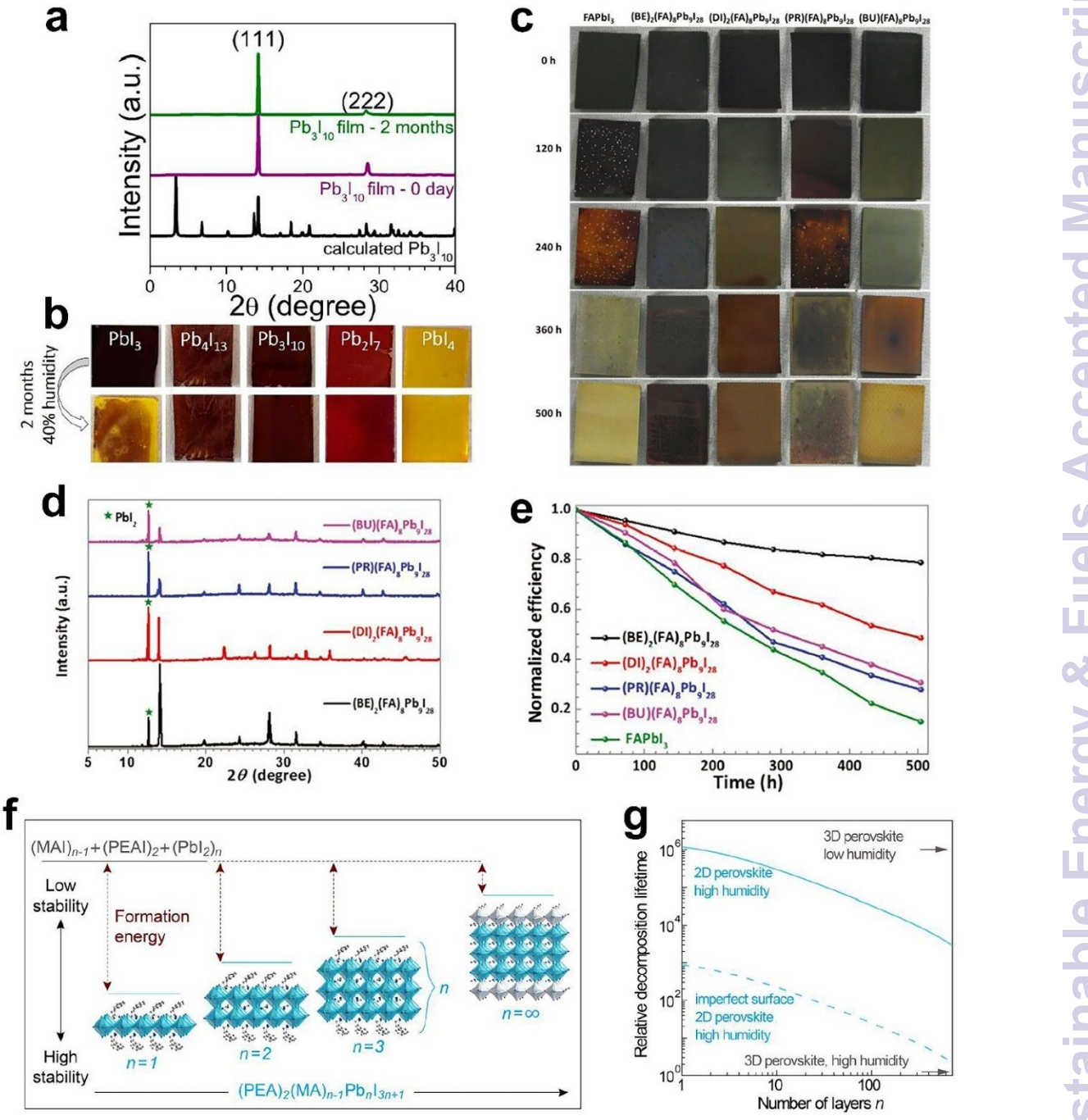

Fig. 11 (a), **(b)** Stability of the $(BA)_2(MA)_{n-1}Pb_nI_{3n+1}$ (n = 1–4, and ∞) series. **(a)** XRD patterns of a fresh and aged (for 2 months) $(BA)_2(MA)_2Pb_3I_{10}$ film. **(b)** Photographs of five different perovskite films before and after exposure to humidity. **(a)**, **(b)** Reproduced with permission from Ref. [68]. Copyright 2015, American Chemical Society. **(c)** Photographs of $FAPbI_3$ and four quasi-2D perovskite films before and after exposure to 80% relative humidity (RH). **(d)** XRD patterns of four unsealed quasi-2D perovskite thin films after exposure to 80% RH. **(e)** Normalized efficiency variation curves of four 2D perovskite and $FAPbI_3$ perovskite single crystals exposed to 80% RH. **(c)–(e)** Reproduced with permission from Ref. [66]. Copyright 2018, Wiley VCH. **(f)**, **(g)** Energetics of perovskite formation and stability. **(f)** Unit cell structure of $(C_8H_9NH_3)_2(CH_3NH_3)_{n-1}Pb_nI_{3n+1}$ perovskites with different n values, showing the evolution of dimensionality from 2D (n = 1) to 3D (n = ∞). **(g)** Density functional theory simulation of the formation energy of perovskites with different n values in different atmospheres. **(f)**, **(g)** Reproduced with permission from Ref. [47]. Copyright 2016, American Chemical Society.

View Article Online
DOI: 10.1039/C9SE01181A

ARTICLE

stability of the 3D perovskite $FAPbI_3$ and four quasi-2D perovskites under the same conditions are shown in Fig. 11c. The 3D $FAPbI_3$ perovskite exhibited evident morphology changes, displaying considerable decomposition after exposure to humid conditions for 120 h, whereas the other four quasi-2D perovskites remained almost unchanged under the same conditions. The hydrophobicities of the four quasi-2D perovskites were different. According to Fig. 11c–e, the humidity stability of the four perovskite thin films displayed the following order: $(PR)(FA)_8Pb_9I_{28}$ < $(BU)(FA)_8Pb_9I_{28}$ < $(DI)_2(FA)_8Pb_9I_{28}$ < $(BE)_2(FA)_8Pb_9I_{28}$. These results correlate with the cation valence state and number of carbon atoms in the organic spacers: the lower the valence state and greater the number of carbon atoms of the organic spacers, the higher the humidity resistance of the films. In addition, a solar cell based on $(BE)_2(FA)_8Pb_9I_{28}$ showed a high PCE of 17.4%. Importantly, this device based on $(BE)_2(FA)_8Pb_9I_{28}$ maintained 80% of its initial PCE after exposure to 80% relative humidity (RH) for 500 h.

The introduction of organic spacers into 3D perovskite structures not only provides hydrophobic groups, but also alters the fairly rigid 3D framework composed of corner-sharing octahedra to an open architecture.[131] As described above, *t* of a perfect perovskite structure lies within the range of 0.9–1.0 and distortion arises when *t* deviates from this range, which increases the instability of the structure. Density functional theory (DFT) was used to simulate the stability of dimensionally tuned perovskites, as presented in Fig. 11f. The calculations indicated that the formation energy of 3D perovskites is quite low, which makes it easy for them to decompose to their precursors, especially in a humid environment. This accounts for the low stability of these materials under ambient conditions.[47] The situation is quite different for the 2D RP phases because the introduction of large organic molecules that are not incorporated into the 3D lattice provide appreciable van der Waals interactions. These interactions greatly ease the structural stress of 3D perovskites and therefore suppress their degradation. Both desorption energies and decomposition lifetimes decrease considerably as *n* increases (Fig. 11g), consistent with the sensitivity of perovskites to moisture. In addition, previous studies have shown that replacing MA^+ with FA^+ further increased the stability of 2D RP phases as well as markedly improving solar cell performance.[124, 132] Therefore, more robust solar cells with outstanding stability can be expected by careful composition engineering.

4. Applications of Ruddlesden–Popper perovskites in highly efficient photodetectors

Apart from their outstanding stability in the ambient environment, 2D hybrid RP perovskites also possess fascinating properties including high absorption coefficient, appropriate and tunable band gap, high carrier mobility, and long charge-diffusion length. These features make 2D hybrid RP perovskites promising candidates for use as highly efficient photodetectors. In this section, recent advances of RP perovskite-based photodetectors are discussed.

View Article Online
DOI: 10.1039/C9SE01181A

ARTICLE

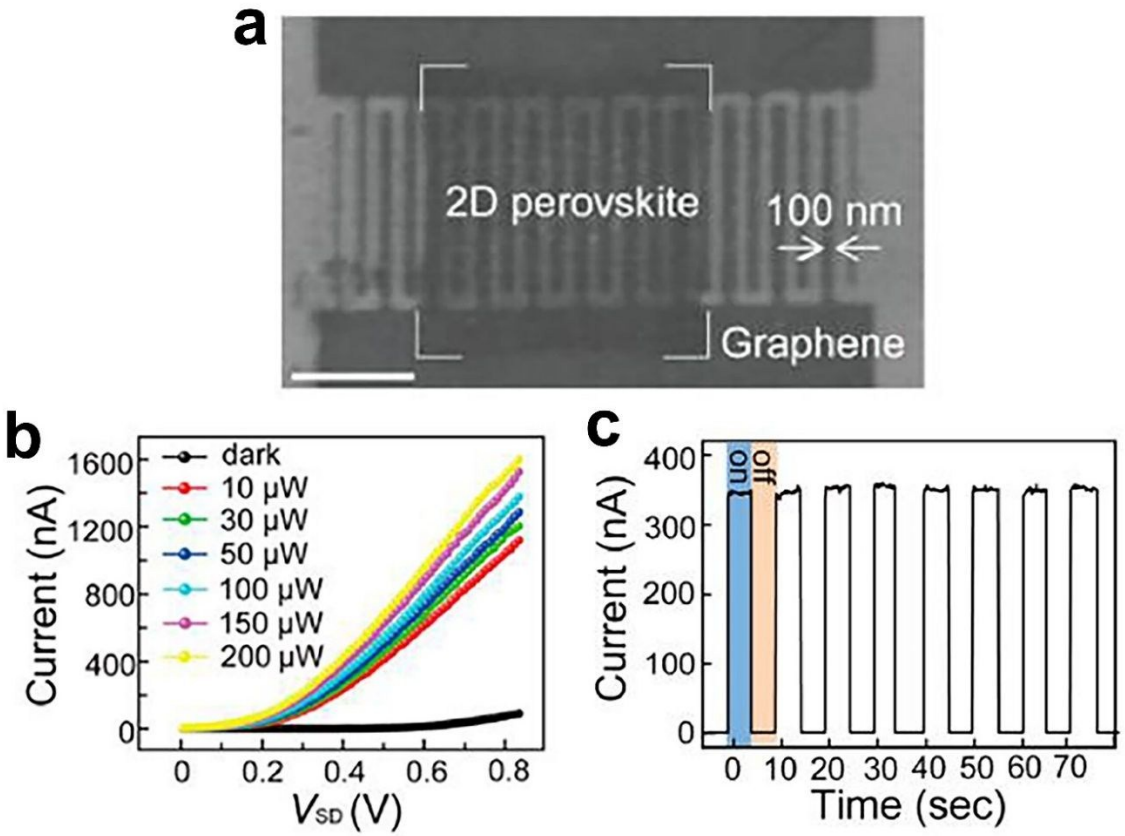

Fig. 12 Photodetectors based on Ruddlesden–Popper phases. **(a)** SEM images of a photodetector based on 2D $(C_4H_9NH_3)_2PbBr_4$. Scale bar, 1 μm. **(b)** Current–voltage (I_{SD}-V_{SD}) curves of the device in the dark and under different illumination intensities of a 470-nm defocused laser. **(c)** Time-dependent photocurrent response of the device exposed to a 470-nm defocused laser with a spot size of 1 mm^2 operated at a bias voltage of 0.5 V and power of 10 μW. Reproduced with permission from Ref. [133]. Copyright 2016, American Chemical Society.

In 2016, Tan and colleagues systematically studied the photodetection performance of $(C_4H_9NH_3)_2PbBr_4$ perovskite.[133] Interdigitated electrodes of graphene with a distance between each pair of graphene electrodes of about 100 nm were designed to increase the absorption cross section of the perovskite (Fig. 12a). Current–voltage (*I*–*V*) curves of the device showed distinct differences in the dark and under discrete illumination intensities of a 470-nm defocused laser (Fig. 12b).The dark current of the device was extremely low (10^{-10} A), whereas the corresponding photocurrent under illumination gradually increased with the incident power. The time-dependent photocurrent response of the device at 470 nm was also investigated (Fig. 12c). An on/off current ratio of nearly 10^3 was obtained under a small bias (0.5 V) and weak incident power (10 μW), leading to an ultrahigh photoresponsivity of up to 2100 A/W. It should be noted that in this study, graphene was introduced during device fabrication and the efficient encapsulation of the perovskite by the graphene electrodes greatly enhanced both the photoresponsivity and robustness of the device.

Ferroelectricity has been used to enhance the photoelectric performance of 2D RP perovskites. Previous studies have shown that the built-in electric field provided by the large spontaneous polarization of ferroelectric materials greatly lowers the dark current, which improves the signal-to-noise ratio and thus photodetection performance.[134, 135] In 2017, Li et al.[115] reported a high-performance photodetector based on an unusual ferroelectric RP phase $(C_4H_9NH_3)_2(CH_3NH_3)_2Pb_3Br_{10}$.

View Article Online
DOI: 10.1039/C9SE01181A

ARTICLE

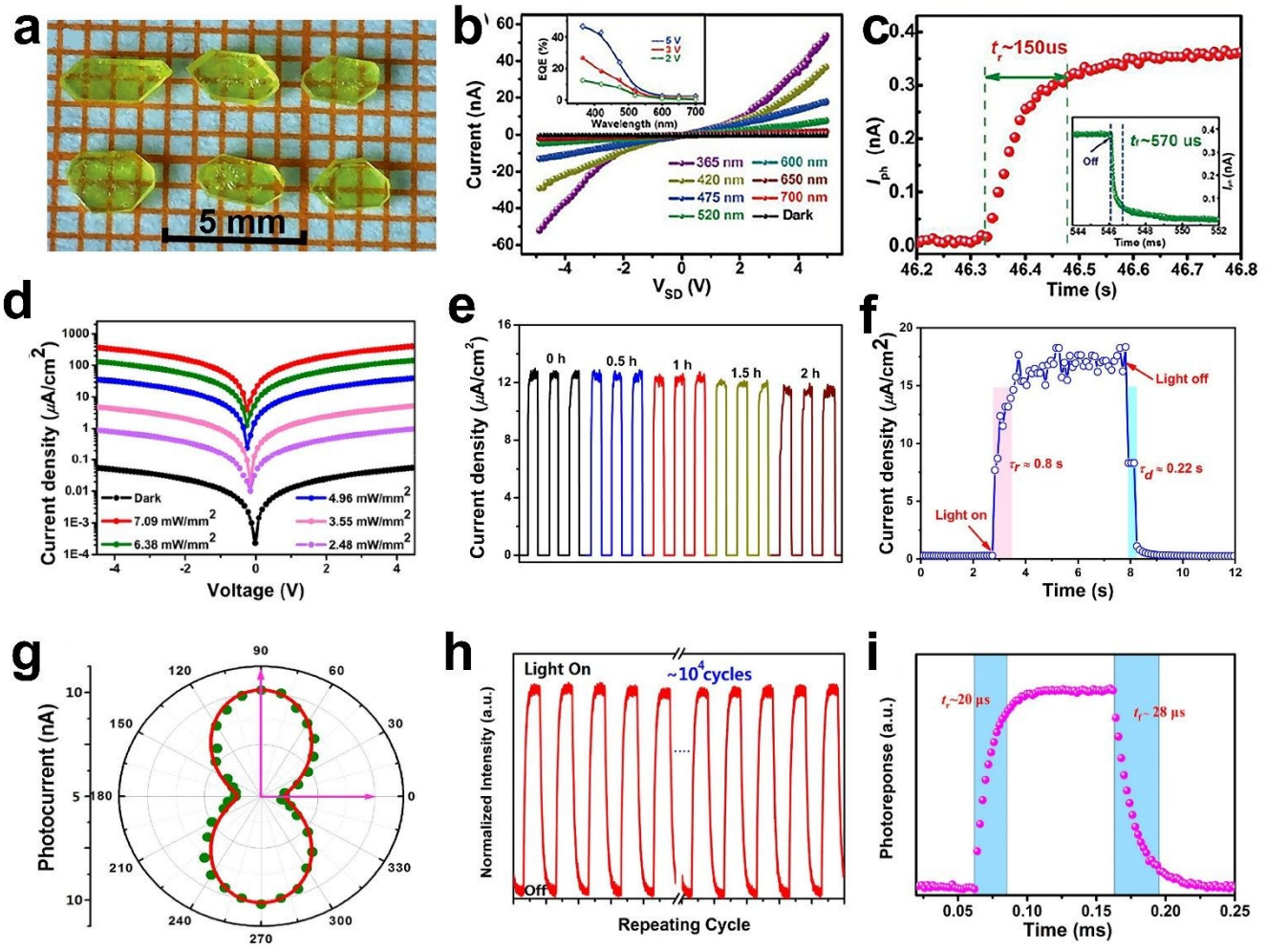

Fig. 13 Photodetectors based on ferroelectric Ruddlesden–Popper (RP) perovskites. **(a)** Photograph of bulk single crystals of $(C_4H_9NH_3)_2(CH_3NH_3)_2Pb_3Br_{10}$ grown by the temperature-cooling method. **(b)** Variation of photocurrent with incident wavelength under a fixed power of about 2.13 mW/cm^2. **(c)** Enlarged view of the rise and fall of photocurrent responses during on-off light switching. **(a)–(c)** Reproduced with permission from Ref. [115]. Copyright 2017, Wiley VCH. **(d)** Current density–voltage (*J-V*) characteristics of a photodetector based on the 2D ferroelectric RP perovskite $EA_4Pb_3Cl_{10}$ in the dark and under 266-nm illumination at different incident powers. **(e)** Time-dependent photocurrent response of the device exposed to ambient conditions. **(f)** The rise and decay of the photocurrent response of the device at zero-bias. **(d)–(f)** Reproduced with permission from Ref. [136]. Copyright 2020, American Chemical Society. **(g)** Polarization dependence of the angle-resolved photocurrent under polarized incident light of a photodetector based on the 2D ferroelectric RP perovskite $(CH_3(CH_2)_3NH_3)_2(CH_3NH_3)Pb_2Br_7$. Along the horizontal axis, the electric field induced by the polarized light is parallel to the crystallographic *a*-axis (in-plane direction). **(h)** Long-term repeated switching cycles illustrating the photoresponse of the device. **(i)** Rise and decay of the photocurrent response of the device. **(g)–(i)** Reproduced with permission from Ref. [137]. Copyright 2019, American Chemical Society.

Perovskite single crystals with high optical quality, as shown in Fig. 13a, were grown by the temperature-cooling method and then a highly oriented wafer was exfoliated from the crystal and used to fabricate a photodetector. Notable photocurrent was observed when the incident wavelength was below 550 nm, which decreased sharply when the incident wavelength was longer than 550 nm (Fig. 13b). The photodetector showed an extremely low dark current (~2×10^{-12} A at 5 V). The on/off ratio of the device was at least 2.5×10^3 and an optimized photodetectivity of 3.6×10^{10} Jones was obtained. The response speed of the device was also measured. Figure 13c shows that the estimated rise (τ_r) and decay (τ_f) times were τ_r = 150 and τ_f = 570 μs, which are faster or comparable to those of reported

photodetectors based on 3D hybrid and all-inorganic perovskites.[138-141]

The spontaneous polarization P_s and large anisotropy of the crystallographic structures of ferroelectric 2D RP perovskites have also inspired scientists to design new self-powered and polarization-sensitive photodetectors.[136, 137, 142] Taking advantage of the ability of the built-in electric field to enhance the separation of photoexcited electron–hole pairs, a self-powered photoresponse was realized using a newly developed 2D ferroelectric perovskite, $(EA)_2(MA)_2Pb_3Br_{10}$ (EA: ethylammonium), which exhibited P_s of 3.7 μC/cm^2.[142] Strikingly, a zero-bias photocurrent of 4.1 μA/cm^2 was obtained for the self-powered photodetector, as well as an ultralarge "on/off" ratio of ~10^6. The responsivity and detectivity of the device were determined to be 1.35 mA/W and 1.16×10^9 Jones, respectively. Recently, the same research group successfully grew a new ferroelectric 2D perovskite, $EA_4Pb_3Cl_{10}$, which exhibited a larger P_s of ~4.5 μC/cm^2 and a wider bandgap of 3.39 eV.[136] Benefiting from the large P_s and bandgap, a self-powered visible-blind ultraviolet photodetector was designed and fabricated. As shown in Fig. 13d, under 266-nm illumination with a fixed incident power of 7.09 mW/mm^2, a zero-bias photocurrent as high as 18.6 μA/cm^2 was obtained. This value is larger than those of most conventional inorganic ferroelectrics and also the previously mentioned 2D RP perovskite $(EA)_2(MA)_2Pb_3Br_{10}$. Figure 13e and f display the time-dependent photocurrent response and τ_r and τ_f of the device, respectively. After 2 h of on/off cycles, only slight degradation was observed. τ_r and τ_f of the device were 0.8 and 0.22 s, respectively. Detailed performance parameters of the photodetector are listed in Table 3.

Combining the ferroelectric spontaneous polarization and strong structural anisotropy of 2D RP perovskites, a polarization-sensitive photodetector working in the short-wavelength region was also prepared based on the 2D RP perovskite $(BA)_2(MA)Pb_2Br_7$, which exhibited a P_s of 3.6 μC/cm^2 and bandgap of ~2.55 eV.[137] Under 405-nm illumination incident from the *b*-axis (in-plane direction), as shown in Fig. 13g, the maximum photocurrent (I_{max}) was reached when the polarization direction of the incident light was parallel to the crystallographic *c*-axis (in-plane direction), whereas the minimum photocurrent (I_{min}) was observed along the *a*-axis (out-of-plane direction). The calculated polarization-dependent dichroism ratio (I_{max}/I_{min}) was ~2.0. These results are in good agreement with the previously reported theoretical analysis of RP materials, which suggest that the large anisotropy of layered perovskites means they exhibit better performance as polarized light detectors than solar absorbers.[70, 71] After long-term repeated "on/off" switching (~10^4 cycles), no obvious fatigue was observed, indicating the photodetector displayed excellent anti-fatigue behavior (Fig. 13h). The photodetector also exhibited highly sensitive detectivity of up to ~10^9 Jones and a fast response speed with measured τ_r and τ_f of ~20 and ~28 μs, respectively (Fig. 13i). This promising performance makes $(BA)_2(MA)Pb_2Br_7$ a potential candidate material for use in short-wavelength polarization-sensitive detection.

In 2018, Leng and co-workers found that laser-induced surface relaxation can be used to modulate the energy landscape in molecularly thin RP phases in a highly reversible manner and $(CH_3(CH_2)_3NH_3)_2(CH_3NH_3)_4Pb_4I_{13}$ showed superior photodetection performance.[116] Bulk single crystals of the $(CH_3(CH_2)_3NH_3)_2(CH_3NH_3)_{n-1}Pb_nI_{3n+1}$ (n = 1–4) family were grown by a temperature-programmed crystallization method. Monolayer, bilayer, and bulk flakes of the n = 4 member were exfoliated from the crystal to fabricate photodetectors. The monolayer and bilayer flakes were treated by laser annealing to form a relaxed state whereas the bulk remained derelaxed. The flakes were electrically contacted by bottom gold contacts and then the device was capped with *h*BN as a protection layer (Fig. 14a). The *I-V* curves of the device (Fig. 14b) revealed that it displayed an ultralow dark current of 10^{-13} A and the photocurrent reached 610 nA at a laser excitation power of 346 μW at a source–drain voltage of 3 V, corresponding to an increase of five orders of magnitude. Figure 14c shows that the photocurrent of the device based on bulk flakes was substantially higher than that of the monolayer one (Fig. 14b), which confirmed that the photocurrent was limited by the density of photosensitive states and excitons were able to tunnel across the layers to dissociate at electrodes, contributing to high responsivity and detectivity. The calculated photodetectivities for the monolayer and bulk flake-based detectors were 4.7×10^{10} and 1.1×10^{12} Jones, respectively. Under focused laser illumination at 532 nm, the calculated photoresponsivities at an excitation power of 36 nW for the monolayer, bilayer, and bulk perovskites were 11.3, 24.2, and 71.9 mA/W, respectively. A responsivity of 7.4×10^4 A/W and ultrahigh photodetectivity of 1.2×10^{15} Jones were obtained using the detector based on bulk flakes with a thickness of around 20 nm under the same laser illumination (Fig. 14d). This promising performance makes these 2D materials attractive for practical applications.

Apart from the strain engineering of RP perovskites to modulate their optoelectronic performance, the fringe effect can also be used to improve the performance of 2D perovskite-based devices. In 2018, 2D-perovskite nanowire arrays of $(BA)_2(MA)_{n1}Pb_nI_{3n+1}$ (n = 2–5) with pure crystallographic orientations were designed and fabricated for use in photodetection.[143] Figure 14e shows the photodetector

View Article Online
DOI: 10.1039/C9SE01181A

ARTICLE

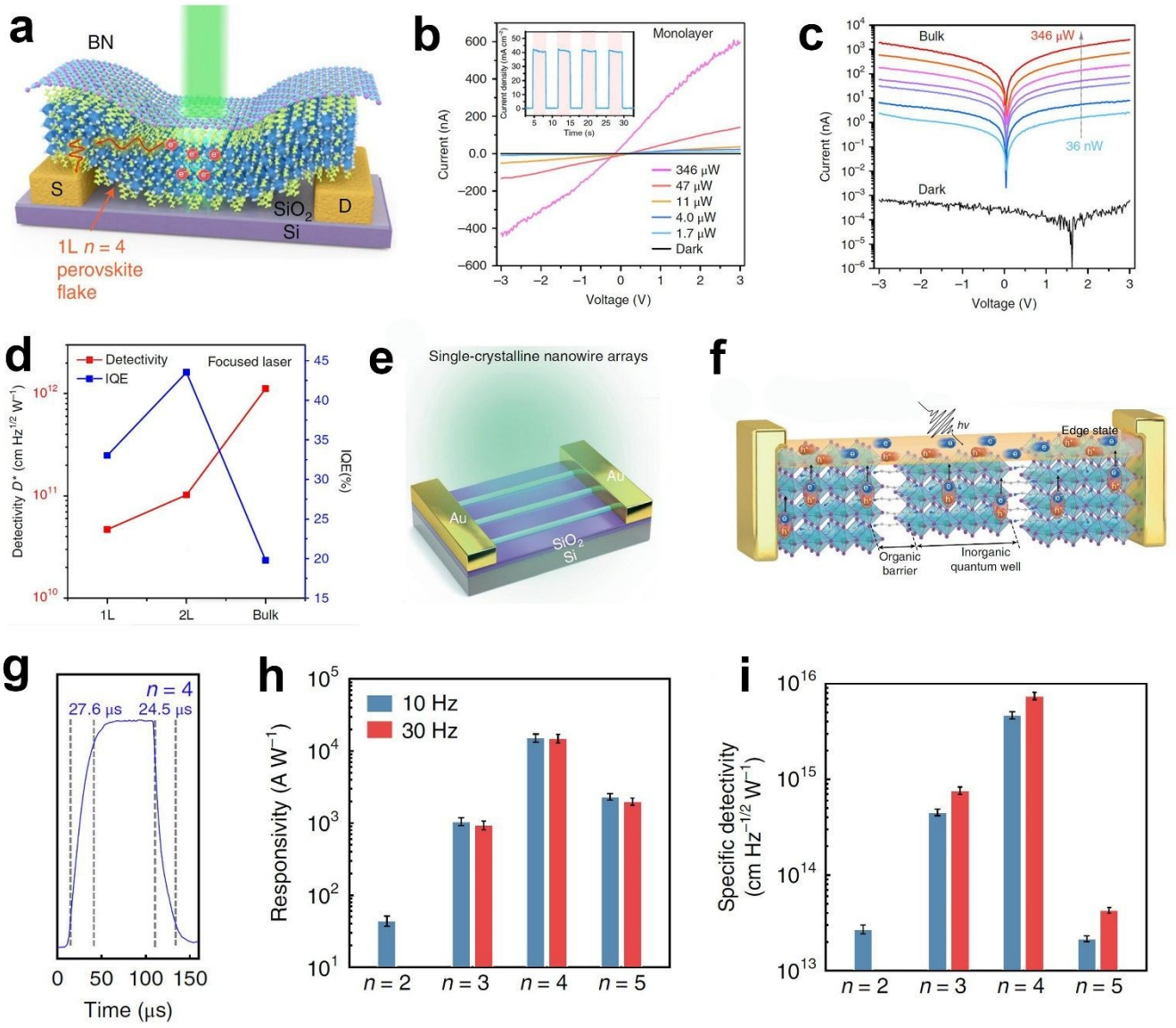

Fig. 14 Photodetectors based on Ruddlesden–Popper (RP) phases. **(a)** Schematic of the structure of a photodetector device based on a monolayer $(CH_3(CH_2)_3NH_3)_2(CH_3NH_3)_3Pb_4I_{13}$ flake. **(b)** *I-V* characteristics of a monolayer perovskite device tested in the relaxed state in the dark and under different illumination intensities. **(c)** *I-V* curves of the bulk device in the dark and under different illumination intensities. **(d)** Comparison of the detectivity D^* and internal quantum efficiency (IQE) of photodetectors made from monolayer, bilayer, and bulk perovskite flakes. **(a)–(d)** Reproduced with permission from Ref. [116]. Copyright 2018, Springer Nature. **(e)** Illustration of a photodetector based on single-crystalline 2D $(BA)_2(MA)_3Pb_3I_{13}$ nanowire arrays. **(f)** Schematic of carrier dynamics in the photodetector of single-crystalline (101)-oriented 2D perovskite. **(g)** Temporal response of 1D arrays of the layered perovskite. **(h)**, **(i)** Responsivities and detectivities, respectively, of n = 2–5 nanowires in the $(BA)_2(MA)_{n-1}Pb_nI_{3n+1}$ series under modulation frequencies of 10 and 30 Hz. **(e)–(i)** Reproduced with permission from Ref. [143]. Copyright 2018, Springer Nature.

structure based on the nanowire arrays. According to electron diffraction results, the nanowires exhibit pure crystallographic orientations because each wire was perpendicular to the perovskite layer and correspondingly, the spatially confined height and width were parallel to the perovskite layer, as shown in Fig. 14f. This device design integrates insulating organic barriers in the carrier-transport pathway to suppress the dark current with a highly photoconductive channel,

provided by the exposed crystalline edges, for exciton dissociation, free-carrier conduction, and charge injection.[144] This structure created high resistance in the interior of the crystals and high conductivity at the edges of the crystals. Using this structure, superior photodetection performance was achieved, especially for the n = 4 material $(BA)_2(MA)_3Pb_4I_{13}$, which exhibited the best overall performance among the perovskites with n = 2–5. Because of the ability of the serial insulating organic barriers in the carrier-transport channel to suppress the dark current, photodetectors fabricated with perovskites with n = 2–4 exhibited quite low dark currents of the order of 10^{-12} A. The response speed of the photodetectors was also impressive. As shown in Fig. 14g, the response times of the photodetector fabricated with the n = 4

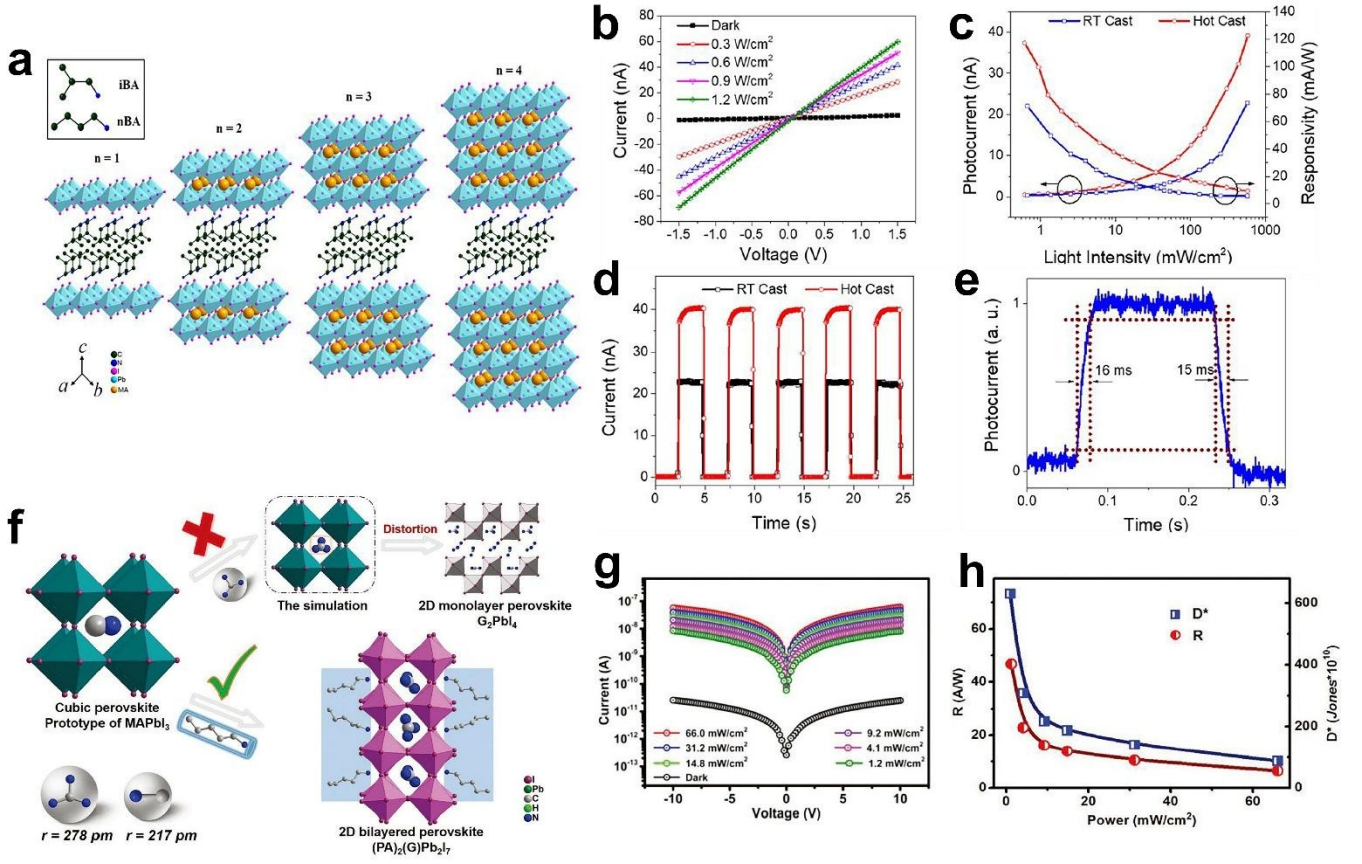

Fig. 15 (a) Schematic illustration of the crystal structure of layered perovskite materials with the chemical formula $(i\text{BA})_2(\text{MA})_{n-1}\text{Pb}_n\text{I}_{3n+1}$ (n = 1–4). Inset are the chemical structures of *i*BA and *n*BA. All hydrogen atoms are omitted. **(b)–(e)** Photoresponse properties of the room-temperature and hot-cast-fabricated samples with the chemical formula $(i\text{BA})_2(\text{MA})_3\text{Pb}_4\text{I}_{13}$. **(b)** *I–V* curves with and without light illumination. **(c)** Photocurrent and responsivity against light intensity. **(d)** Current vs. time under modulated incident light. **(e)** High-resolution current vs. time curve. In **(c)–(e)**, the bias voltage was 1.5 V and the incident light wavelength was 532 nm. In **(d)** and **(e)**, the light intensity was 0.6 W/cm². **(a)–(e)** Reproduced with permission from Ref. [145]. Copyright 2018, American Chemical Society. **(f)** Illustration of the tailored design of $(PA)_2(G)Pb_2I_7$. Because of the tolerance-factor restriction, it fails to directly insert a large G cation into the perovskite cavity confined by the corner-sharing PbI_6 octahedra. However, for $(PA)_2(G)Pb_2I_7$, organic G cations can be located inside the distorted perovskite framework as a "perovskiter" to form a 2D bilayer perovskite motif. **(g)** I_{ph} and I_{dark} measured under different incident light power intensities. **(h)** Photoresponsivity R and detectivity D^* of $(PA)_2(G)Pb_2I_7$ as a function of incident light power. **(f)–(h)** Reproduced with permission from Ref. [118]. Copyright 2019, Wiley VCH.

perovskite were τ_r = 27.6 μs and τ_f = 24.5 μs under an irradiance of 229 mW/cm². The photoresponsivities and detectivities of the photodetectors were also evaluated. The n = 4 perovskite nanowires presented high average responsivities of $(1.53\pm0.19)\times10^4$ and $(1.51\pm0.21)\times10^4$ A/W at modulation frequencies of 10 and 30 Hz, respectively, corresponding to detectivities of $(4.68\pm0.41)\times10^{15}$ and $(7.45\pm0.66)\times10^{15}$ Jones, respectively (Fig. 10h and i).

Apart from modulating the photodetector performance by modifying the surface state of the materials, introducing a built-in electric field to suppress the dark current, or using fringe effects, some other ways have also been developed to regulate their performance. Recently. Dong et al.[145] reported the synthesis of quasi-2D RP perovskite $(i\text{BA})_2(\text{MA})_{n-1}\text{Pb}_n\text{I}_{3n+1}$ by replacing the frequently used linear *n*-butylamine (BA) with short-branched iso-butylamine (*i*BA), which is an isomer of BA, as shown in Fig. 15a. Using *i*BA, enhanced photodetection performance was achieved. Two different approaches, room-temperature casting and hot casting, were used in the material synthesis. The hot-casting method was found to be preferable for the material synthesis, yielding enhanced photodetection performance including a responsivity as high as 117.09 mA/W, on/off ratio of 4.0×10^2, and responses of τ_r = 16 ms and τ_f = 15 ms for the n = 4 perovskite in the $(i\text{BA})_2(\text{MA})_{n-1}\text{Pb}_n\text{I}_{3n+1}$ series

View Article Online
DOI: 10.1039/C9SE01184A

(Fig. 15b–e). In addition to the modification of the organic spacer, attempts have been made to replace the so-called "perovskiter" site, which is located within the PbI_3 perovskite framework and usually occupied by MA^+.[146-150] Recently, Dong and colleagues incorporated mixed cations like FA^+ and Cs^+ into $(iBA)_2(MA)_3Pb_4I_{13}$ and designed a new series of photodetectors.[150] After detailed measurements and analysis, $(iBA)_2((MA_{0.4}FA_{0.6})_{0.9}Cs_{0.1})_3Pb_4I_{13}$ ($FA_{0.6}Cs_{0.1}$) was found to show the best photodetection performance of the doped materials. Flexible photodetectors based on $FA_{0.6}Cs_{0.1}$ were fabricated and exhibited attractive performance, including high detectivity up to 1.68×10^{12} Jones, acceptable responsivity of 400 mA/W, and fast responses of τ_r = 43 ms and τ_f = 22 ms. Detailed performance parameters of the photodetector are listed in Table 3.

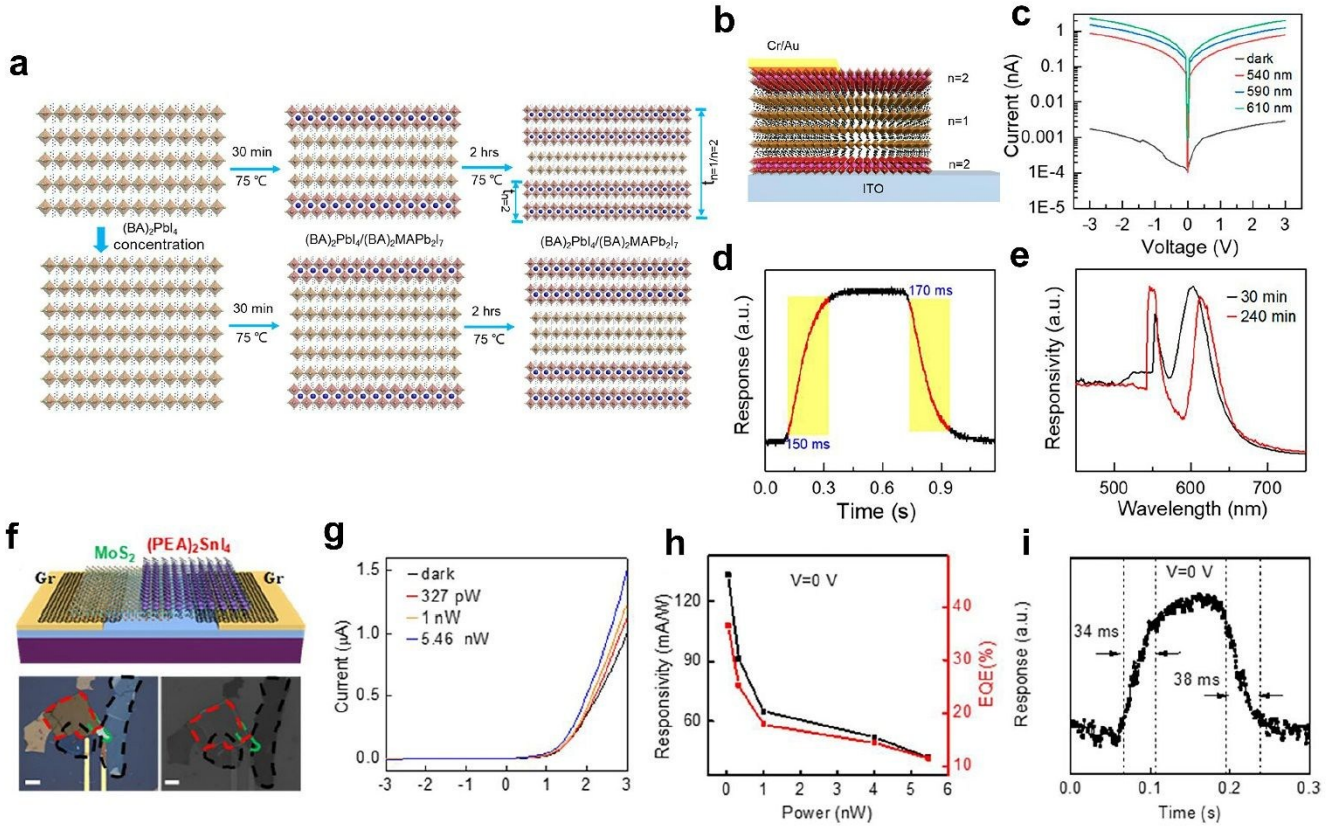

Fig. 16 (a) Schematic illustration of the growth process of centimeter-sized $(BA)_2PbI_4/(BA)_2(MA)Pb_2I_7$ heterostructures. **(b)** Schematic illustration of the narrow dual-band photodetector configuration of the $(BA)_2PbI_4/(BA)_2(MA)Pb_2I_7$ heterostructure. **(c)** Output characteristics (*I–V* curves) of the heterostructured device in the dark and under different monochromatic light illumination conditions. **(d)** Temporal photoresponse of the $(BA)_2PbI_4/(BA)_2(MA)Pb_2I_7$ heterostructured photodetector irradiated by 540-nm light with a power density of 45 mW/cm^2 under a bias voltage of 3 V. **(e)** Normalized responsivity of narrow dual-band $(BA)_2PbI_4/(BA)_2(MA)Pb_2I_7$ heterostructure photodetectors fabricated with maintaining times of 30 and 240 min (corresponding to $(BA)_2(MA)Pb_2I_7$ layer thicknesses of 300 nm and 1.1 μm, respectively) under a bias voltage of 3 V. **(a)–(e)** Reproduced with permission from Ref. [105]. Copyright 2019, American Chemical Society. **(f)** Schematic illustration, optical microscopy image, and SEM image of the as-fabricated graphene/$(PEA)_2SnI_4/MoS_2$/graphene device. The scale bar represents 20 μm. **(g)** I_{ds}–V_{ds} curves of the graphene/$(PEA)_2SnI_4/MoS_2$/graphene device under 451-nm light at different intensities. **(h)** Power-dependent responsivity and external quantum efficiency (EQE) of the as-prepared graphene/$(PEA)_2SnI_4/MoS_2$/graphene device at zero bias. **(i)** Transient photocurrent response at zero bias. The incident light power was 5.46 nW. **(f)–(i)** Reproduced with permission from Ref. [151]. Copyright 2019, American Chemical Society.

Apart from the traditional organic MA^+ and FA^+ and inorganic Cs^+, there are also some other monovalent organic groups that can act as the perovskiter. As depicted in Fig. 15f, the relatively large guanidinium (G) group was first introduced into $(PA)_2(G)Pb_2I_7$ (PA = n-pentylaminium) as the perovskiter.[118] Single-crystal array photodetectors based on the obtained materials were fabricated that achieved high photodetectivities (6.3×10^{12} Jones) and responsivities (~47 A/W), as well as low dark current (~2.4×10^{-11} A) (Fig. 15g and h). The outstanding performance of the $(PA)_2(G)Pb_2I_7$-based photodetectors paves the way to explore novel 2D hybrid perovskite candidates to improve the performance of optoelectronic devices.

Heterostructures are of great importance in advanced electronics because of their ability to exhibit physical properties inaccessible to single-material systems. Thus, heterostructures can tremendously extend the functionalities of electronic devices.[152] In particular, 3D perovskite-based heterostructures have been widely studied and numerous achievements have been realized.[36, 153-157] Compared with their 3D counterparts, the 2D structural characteristics and van der Waals interactions between the organic spacer layer and

Journal Name ARTICLE

View Article Online
DOI: 10.1039/C9SE01181A

perovskite-like layers of RP phases make these materials perfect candidates for high-performance photodetectors with low noise because of their lack of dangling bonds.[81, 158] Therefore, integrating RP perovskites into heterostructures has attracted intense attention, although this field is still in its infancy. Recently, $(C_4H_9NH_3)_2PbI_4/(C_4H_9NH_3)_2(CH_3NH_3)Pb_2I_7$ and $(PEA)_2SnI_4/MoS_2$ heterostructures were prepared for use in photodetectors.[105, 151] As shown in Fig. 16a, a centimeter-sized $(C_4H_9NH_3)_2PbI_4/(C_4H_9NH_3)_2(CH_3NH_3)Pb_2I_7$ heterostructure, in which the n = 2 perovskite layer grew outside that with n = 1, was successfully grown by optimizing the precursor concentration and maintaining time. Based on the heterostructure, a two-probe vertical electronic device was designed. Figure 16b shows that the fabricated device consisted of two back-to-back heterostructures, which greatly

Table 3 Performances of some photodetectors based on Ruddlesden–Popper perovskites.

Materials	Dark current (A)	On/off ratio	Responsivity (A/W)	Detectivity (Jones)	Response speed	Test conditions	Ref.
$(BA)_2PbBr_4$	~10^{-10}	10^3	~2100	-	-	λ: 470 nm; V_{bias}: 0.5 V; P_{inc}: 10 μW	133
$(BA)_2PbI_4$	1×10^{-12} ~ 1×10^{-11}	1×10^2 (V_{bias}: 10 V)	3.0×10^{-3}	-	τ_r: 28.4 ms; τ_f: 27.5 ms	V_{bias}: 30 V; P_{inc}: 3.0 mW/cm^2	159
$(BA)_2(MA)Pb_2I_7$			7.31×10^{-3}	-	τ_r: 8.4 ms; τ_f: 7.5 ms		
$(BA)_2(MA)_2Pb_3I_{10}$		1×10^3 (V_{bias}: 10 V)	12.78×10^{-3}	-	τ_r: 10.0 ms; τ_f: 7.5 ms		
$(BA)_2(MA)_{n-1}Pb_nBr_{3n+1}$	2.8×10^{-12}	2.3×10^3 (4.63 mW/cm^2)	190×10^{-3} (500 nm, 0.33 mW/cm^2)	-	τ_r: 0.21 s; τ_f: 0.24 s (532 nm, 0.42 mW/cm^2)	V_{bias}: 1 V	160
$(BA)_2(MA)_2Pb_3Br_{10}$	10^{-12}	2.5×10^3		3.6×10^{10}	τ_r: 150 μs; τ_f: 7.5 μs	λ: 420 nm; V_{bias}: 5 V P_{inc}: 2.13 mW/cm^2	115
$(BA)_2MAPb_2Br_7$ unpolarized		~1.2×10^3				λ: 405 nm	137
$(BA)_2MAPb_2Br_7$ Polarized (c-axis)				~1.1×10^9	τ_r: ~20 μs; τ_f: ~28 μs		
$EA_4Pb_3Cl_{10}$		~10^4	26.2×10^{-6}	3.06×10^9	τ_r: ~0.8 s; τ_f: ~0.22 s	λ: 266 nm; V_{bias}: 0 V; P_{inc}: 2.48 mW/mm^2	136
$(EA)_2(MA)_2Pb_3Br_{10}$	~4×10^{-15}	~10^6	1.35×10^{-3}	1.16×10^9	τ_r: ~96 μs; τ_f: ~123 μs	λ: 405 nm; V_{bias}: 0 V; P_{inc}: 0.1 W/cm^2	142
$(OA)_2FA_{n-1}Pb_nBr_{3n+1}$			32		τ_r: 0.25 ms; τ_f: 1.45 ms	λ: 442 nm V_{bias}: 9 V P_{inc}: 3.2 mW/mm^2	146
$(iBA)_2(MA)_3Pb_4I_{13}$ (hot casting treated)	1.3×10^{-11} ~ 3.1×10^{-9}	4.0×10^2	117.09×10^{-3}		τ_r: 16 ms; τ_f: 15 ms	λ: 532 nm; V_{bias}: 1.5 V; P_{inc}: 0.6 W/cm^2	145
$(iBA)_2(MA)_3Pb_4I_{13}$		4.1×10^2	71.11×10^{-3}		τ_r: ~20 ms; τ_f: 17 ms		
$(iBA)_2((MA_{0.4}FA_{0.6})_{0.9}Cs_{0.1})_3Pb_4I_{13}$	1.27×10^{-12}	720	400×10^{-3}	1.68×10^{12}	τ_r: ~43 ms; τ_f: ~22 ms	λ: 532 nm; V_{bias}: 1.5 V; P_{inc}: 0.22 W/cm^2	150
$(iBA)_2PbI_4$	2×10^{-10}		0.56	1.23×10^{10}	τ_r: ~233 ms; τ_f: ~166 ms	λ: 560 nm; V_{bias}: -5 V;	161

BA: butylamine; MA: methylamine; EA: ethylammonium; OA: octadecylamine; FA: formamidine; (*i*BA): iso-butylamine; PEA: phenylethylamine; PA: n-pentylamine; G: guanidinium.

continued

Materials	Dark current (A)	On/off ratio	Responsivity (A/W)	Detectivity (Jones)	Response speed	Test conditions	Ref.
$(BA)_2(MA)_3Pb_4I_{13}$	$< 10^{-12}$		$(1.53 \pm 0.19) \times 10^4$ (10 Hz) $(1.51 \pm 0.21) \times 10^4$ (30 Hz)	$(4.68 \pm 0.41) \times 10^{15}$ (10 Hz) $(7.45 \pm 0.66) \times 10^{15}$ (30 Hz)	τ_r: 27.6 μs τ_f: 24.5 μs	V_{bias}: 5 V P_{inc}: 229 mW/cm^2	143
$(PA)_2(MA)Pb_2I_7$	1.1×10^{-10}	$> 10^3$	3.87×10^{-3} (P_{inc} = 8 mW/cm^2)	2.92×10^{10} (P_{inc} = 8 mW/cm^2)	τ_r: 1.52 μs τ_f: 1.67 μs	λ: 600 nm V_{bias}: 9.5 V P_{inc}: 35 mW/cm^2	162
$(BA)_2(MA)_3Pb_4I_{13}$ Monolayer	10^{-13}	$> 10^5$ (346 μW, 3V)	11.3×10^{-3} (36 nW)	4.7×10^{10}		Focused laser, λ: 532 nm	116
$(BA)_2(MA)_3Pb_4I_{13}$ Bilayer		-	24.2×10^{-3} (36 nW)				
$(BA)_2(MA)_3Pb_4I_{13}$ Bulk		-	71.9×10^{-3} (36 nW)	1.1×10^{12}			
		-	7.4×10^4	1.2×10^{15}		Defocused laser, λ: 532 nm	
$(PEA)_2MA_3Pb_4I_{13}$	1.7×10^{-4} mA/cm^2	2×10^4 (white light, 62 mW/cm^2)	0.46	6×10^{11}	τ_r: 5.8 ms τ_f: 4.6 ms	λ: 600 nm P_{inc}: 39 μW/cm^2	163
$(PEA)_2SnI_4/MoS_2$	-	10^2 (0 V, 5.46 nW)	0.121 (0 V, 451 nm, 36 pW) 1100 (3 V)	8.09×10^9 (660 nm, 0.5 V)	τ_r: 34 ms τ_f: 38 ms (0 V)	λ: 451 nm	151
$(BA)_2PbI_4$	5.72×10^{-13}	24				V_{bias}: 1 V	164
$(BA)_2(MA)Pb_2I_7$	2.25×10^{-13}	399	2.96	2.7×10^{13}	< 4 ms		
$(BA)_2(MA)_2Pb_3I_{10}$	1.45×10^{-14}	2862					
$(PEA)_2PbI_4$ (001)-plane	3.06×10^{-12}		139.6	1.89×10^{15}	τ_r: 21 μs τ_f: 37 μs	V_{bias}: 5 V P_{inc}: 3.3×10^{-5} mW/cm^2	122
$(BA)_2PbI_4/(BA)_2(MA)Pb_2I_7$	~ 10^{-12}	~10^3	0.69 (540 nm) 0.65 (610 nm)		τ_r: 150 ms τ_f: 170 ms	λ: 540 nm V_{bias}: 3 V P_{inc}: 45 mW/cm^2	105
$(BA)_2PbI_4/(BA)_2(MA)Pb_2I_7$		10^3	~10^{-7}		τ_r: 124 ms τ_f: 110 ms	λ: 980 nm; V_{bias}: 1 V; P_{inc}: 200 mW/cm^2	106
$(PA)_2(G)Pb_2I_7$	~2.4×10^{-11}	2500	47	6.3×10^{12}	3.1 ns	V_{bias}: 10 V P_{inc}: 1.2 mW/cm^2	118

BA: butylamine; MA: methylamine; EA: ethylammonium; OA: octadecylamine; FA: formamidine; (*i*BA): iso-butylamine; PEA: phenylethylamine; PA: n-pentylamine; G: guanidinium.

suppressed the dark current and thus improved the sensitivity of the device to achieve superior photodetection performance. An extremely low dark current of ~10^{-12} A (Fig. 16c), corresponding to a dark current density of 10^{-6} A/cm^2, was obtained and the measured responses were τ_r = 150 ms and τ_f = 170 ms (Fig. 16d). The relatively low response speeds should be attributed to the large thickness of the plate and low operating electric field. A device based on a heterostructure with a thinner n = 2 perovskite layer was also fabricated. This device exhibited a narrow dual-band spectral response with central peaks located at 540 and 610 nm, as shown in Fig. 16e.

Integrating RP perovskites with other 2D layered materials, such as transition metal dichalcogenides and graphene, has also been explored. As shown in Fig. 16f, using few-layer graphene flakes as the electrodes, photodetectors with the structure graphene/$(PEA)_2SnI_4$/MoS_2/graphene were designed and fabricated in which MoS_2 and $(PEA)_2SnI_4$ acted as n-type and p-type semiconductors, respectively. *I-V* curves of the device in the dark and under 451-nm illumination (Fig. 16g) exhibited a rectification ratio as high as 500, more than two orders of magnitude larger than that of 3D perovskite/transition metal dichalcogenide hererostructures.[165-167] Additionally, a responsivity of 1100 A/W at a bias of 3 V (Fig. 16h) and fast response speeds of τ_r = 34 ms and τ_f = 38 ms (Fig. 16i) were obtained for the device, rendering graphene/$(PEA)_2SnI_4$/MoS_2/graphene heterostructures competitive candidates for novel optoelectronics in photodetection, solar cells, and light emission.

Performance parameters, including dark current, on/off ratio, response speed, responsivities, and detectivities, of some RP phase-based photodetectors under different test conditions are compared in Table 3. Although lots of research achievements have already been obtained, the study of 2D RP perovskite-based photodetectors is still in its infancy and further in-depth explorations, especially of devices based on ultrathin and highly oriented single crystals or heterostructures, are still required.

5. Conclusions and outlook

In this review, recent progress of the photodetection applications of 2D RP perovskite materials was summarized. Compared with 3D perovskites like $MAPbI_3$, 2D RP phases exhibit unique properties such as higher ambient stability intrinsic quantum well structure, strong quantum and dielectric confinement effects, and extremely large exciton binding energy. The crystallographic structure of RP perovskites can be regarded as the periodic splitting of 3D perovskites by long-chain organic alkylamine or arylamine spacers. Herein, the structures of 2D RP phases and 3D perovskites were compared to gain further insights into their structure–property relationships. Specifically, the introduction of the relatively large alkylamine or arylamine organic spacers into the crystal structure alters t and prevents the formation of ideal perovskite structure. Instead, a layered structure of perovskite-like layers and organic spacer layers forms. The open layered architecture endows RP phases with high tunability while retaining the advantages of 3D perovskites. The favorable characteristics of RP phases suggest their promise for application in optoelectronics like efficient photodetectors. In this review, different preparation methods of RP phases, including solution-based spin-coating, colloidal-based, liquid- and vapor-phase epitaxy, and exfoliation methods, were discussed. The enhanced stability of RP phases compared with that of 3D perovskites was also reviewed. The relatively large organic spacers not only provide hydrophobic protection of moisture-vulnerable small cations like MA^+, but also introduce a substantial amount of van der Waals interactions into the structure, which eliminates dangling bonds and lessens the structural stress of the perovskite layers, thus improving the ambient stability of RP phases. Considering their outstanding properties, RP phases have attracted wide attention from optoelectronics researchers. Recent advances of photodetectors containing RP phases were also discussed in detail. Because of the ability of the insulating organic spacer layers to suppress the dark current, RP phases exhibit outstanding photodetection performance with detectivity reaching as high as 10^{15} Jones[122, 143], making these materials promising candidates for the development of novel photodetectors.

Unfortunately, the introduction of organic groups into the 3D perovskite structure does not yield only positive effects. There are still obstacles that need to be overcome for the wide application of RP phases, although promising research achievements have been obtained. First, it remains important to develop new members and enlarge the family of RP phases, even though a considerable number of materials have already been identified. Because of their unique open crystal structure, property modulation of RP phases can be easily implemented through proper modification of the organic spacer groups (A site), bivalent metal cations (B site), or halogens (X site). Besides, the traditional pervoskiter motif located inside the perovskite framework, usually MA^+, can also be replaced by the FA^+ or G^+, which further increases the diversity of RP phases.

Second, the overall device performance greatly relies on the quality of the materials, However, the precise control of the composition and phase purity of the synthesized RP materials, especially the large-scale production of high-quality ultrathin flakes, is still difficult. Therefore, additional research effort is needed to study the thermodynamics of the nucleation and growth mechanism of RP phases. Their synthesis methods also need to be developed, modified, or further optimized.

Third, heterostructures of RP phases with other 2D or 3D materials, especially with graphene, disulfide compounds, or 3D perovskites, are urgently needed to extend the functionality of RP phases in optoelectronics. The mechanisms underlying the charge carrier transport and electronic coupling at the interface in such heterostructures should also be elucidated. In addition, there are only a few reports on the

growth of bulk single crystals of RP phases at present.[117, 118, 120-122, 130] Bulk single crystals are necessary because of their irreplaceable role in the study of the anisotropic properties of RP materials and can also provide further insight into the structural origins of their electronic properties. Therefore, it is important to continue to investigate the growth of bulk single crystals of RP phases. Through detailed study and careful selection of the crystallographic orientations, devices with better performance could be rationally designed.

In summary, 2D RP phases have unique open structures and exhibit fascinating optoelectronic properties, which are favorable for their application in devices like highly efficient photodetectors. Although promising achievements have already been obtained, the mechanism of their charge carrier transport dynamics is still unclear and their controlled synthesis is still challenging. In view of the promising application potential of RP phases in optoelectronics, further in-depth study of these materials in the near future is anticipated.

Conflicts of interest

There are no conflicts to declare.

Acknowledgments

The authors gratefully appreciate the financial support from the Natural Science Foundation of Shandong Province (Grant No. ZR2019BEM029).

References

1. A. Kojima, K. Teshima, Y. Shirai and T. Miyasaka, *J. Am. Chem. Soc.*, 2009, **131**, 6050-6051.
2. Z. Zhao, F. Gu, H. Rao, S. Ye, Z. Liu, Z. Bian and C. Huang, *Adv. Energy Mater.*, 2019, **9**, 1802671.
3. Y. Fu, F. Meng, M. B. Rowley, B. J. Thompson, M. J. Shearer, D. Ma, R. J. Hamers, J. C. Wright and S. Jin, *J. Am. Chem. Soc.*, 2015, **137**, 5810-5818.
4. N. Li, Z. Zhu, C.-C. Chueh, H. Liu, B. Peng, A. Petrone, X. Li, L. Wang and A. K. Y. Jen, *Adv. Energy Mater.*, 2017, **7**, 1601307.
5. X. Zheng, Y. Deng, B. Chen, H. Wei, X. Xiao, Y. Fang, Y. Lin, Z. Yu, Y. Liu, Q. Wang and J. Huang, *Adv. Mater.*, 2018, **30**, 1803428.
6. *National Renewable Energy Laboratory, https://www.nrel.gov/pv/assets/pdfs/best-research-cell-efficiencies.20191106.pdf*, 2019.
7. L. Shen, Y. Fang, D. Wang, Y. Bai, Y. Deng, M. Wang, Y. Lu and J. Huang, *Adv. Mater.*, 2016, **28**, 10794-10800.
8. L. Dou, Y. M. Yang, J. You, Z. Hong, W. H. Chang, G. Li and Y. Yang, *Nat. Commun.*, 2014, **5**, 5404.
9. L. Ji, H. Y. Hsu, J. C. Lee, A. J. Bard and E. T. Yu, *Nano Lett.*, 2018, **18**, 994-1000.
10. C. Lan, R. Dong, Z. Zhou, L. Shu, D. Li, S. Yip and J. C. Ho, *Adv. Mater.*, 2017, **29**, 1702759.
11. P. Wangyang, C. Gong, G. Rao, K. Hu, X. Wang, C. Yan, L. Dai, C. Wu and J. Xiong, *Adv. Opt. Mater.*, 2018, **6**, 1701302.
12. Y. H. Kim, H. Cho, J. H. Heo, T. S. Kim, N. Myoung, C. L. Lee, S. H. Im and T. W. Lee, *Adv. Mater.*, 2015, **27**, 1248-1254.
13. W. Deng, H. Fang, X. Jin, X. Zhang, X. Zhang and J. Jie, *J. Matter. Chem. C*, 2018, **6**, 4831-4841.
14. X. Zhang, H. Liu, W. Wang, J. Zhang, B. Xu, K. L. Karen, Y. Zheng, S. Liu, S. Chen, K. Wang and X. W. Sun, *Adv. Mater.*, 2017, **29**, 1606405.
15. A. B. Wong, M. Lai, S. W. Eaton, Y. Yu, E. Lin, L. Dou, A. Fu and P. Yang, *Nano Lett.*, 2015, **15**, 5519-5524.
16. M. R. Leyden, L. Meng, Y. Jiang, L. K. Ono, L. Qiu, E. J. Juarez-Perez, C. Qin, C. Adachi and Y. Qi, *J. Phys. Chem. Lett.*, 2017, **8**, 3193-3198.
17. J. Choi, J. S. Han, K. Hong, S. Y. Kim and H. W. Jang, *Adv. Mater.*, 2018, **30**, 1704002.
18. J. Wang, S. P. Senanayak, J. Liu, Y. Hu, Y. Shi, Z. Li, C. Zhang, B. Yang, L. Jiang, D. Di, A. V. Ievlev, O. S. Ovchinnikova, T. Ding, H. Deng, L. Tang, Y. Guo, J. Wang, K. Xiao, D. Venkateshvaran, L. Jiang, D. Zhu and H. Sirringhaus, *Adv. Mater.*, 2019, **31**, 1902618.
19. S. P. Senanayak, B. Yang, T. H. Thomas, N. Giesbrecht, W. Huang, E. Gann, B. Nair, K. Goedel, S. Guha, X. Moya, C. R. McNeill, P. Docampo, A. Sadhanala, R. H. Friend and H. Sirringhaus, *Sci. Adv.*, 2017, **3**, e1601935.
20. Y. H. Lin, P. Pattanasattayavong and T. D. Anthopoulos, *Adv. Mater.*, 2017, **29**, 1702838.
21. Y. Dang, C. Zhong, G. Zhang, D. Ju, L. Wang, S. Xia, H. Xia and X. Tao, *Chem. Mater.*, 2016, **28**, 6968-6974.
22. D. Ju, Y. Dang, Z. Zhu, H. Liu, C.-C. Chueh, X. Li, L. Wang, X. Hu, A. K. Y. Jen and X. Tao, *Chem. Mater.*, 2018, **30**, 1556-1565.
23. D. Ju, X. Zheng, J. Yin, Z. Qiu, B. Türedi, X. Liu, Y. Dang, B. Cao, O. F. Mohammed, O. M. Bakr and X. Tao, *ACS Energy Lett.*, 2018, **4**, 228-234.
24. D. Yang, X. Zhou, R. Yang, Z. Yang, W. Yu, X. Wang, C. Li, S. Liu and R. P. H. Chang, *Energ. Environ. Sci.*, 2016, **9**, 3071-3078.
25. D. Shi, V. Adinolfi, R. Comin, M. Yuan, E. Alarousu, A. Buin, Y. Chen, S. Hoogland, A. Rothenberger, K. Katsiev, Y. Losovyj, X. Zhang, P. A. Dowben, O. F. Mohammed, E. H. Sargent and O. M. Bakr, *Science*, 2015, **347**, 519-522.
26. V. D'Innocenzo, G. Grancini, M. J. Alcocer, A. R. Kandada, S. D. Stranks, M. M. Lee, G. Lanzani, H. J. Snaith and A. Petrozza, *Nat. Commun.*, 2014, **5**, 3586.
27. A. Marchioro, J. Teuscher, D. Friedrich, M. Kunst, R. van de Krol, T. Moehl, M. Grätzel and J.-E. Moser, *Nat. Photonics*, 2014, **8**, 250-255.
28. C. Wehrenfennig, G. E. Eperon, M. B. Johnston, H. J. Snaith and L. M. Herz, *Adv. Mater.*, 2014, **26**, 1584-1589.
29. T. Leijtens, S. D. Stranks, G. E. Eperon, R. Lindblad, E. M. Johansson, I. J. McPherson, H. Rensmo, J. M. Ball, M. M. Lee and H. J. Snaith, *ACS Nano*, 2014, **8**, 7147-7155.
30. G. Xing, N. Mathews, S. Sun, S. S. Lim, Y. M. Lam, M. Gratzel, S. Mhaisalkar and T. C. Sum, *Science*, 2013, **342**, 344-347.
31. S. D. Stranks, G. E. Eperon, G. Grancini, C. Menelaou, M. J. Alcocer, T. Leijtens, L. M. Herz, A. Petrozza and H. J. Snaith, *Science*, 2013, **342**, 341-344.

32. D. W. deQuilettes, S. M. Vorpahl, S. D. Stranks, H. Nagaoka, G. E. Eperon, M. E. Ziffer, H. J. Snaith and D. S. Ginger, *Science*, 2015, **348**, 683-686.
33. Q. Dong, Y. Fang, Y. Shao, P. Mulligan, J. Qiu, L. Cao and J. Huang, *Science*, 2015, **347**, 967-970.
34. A. A. Zhumekenov, M. I. Saidaminov, M. A. Haque, E. Alarousu, S. P. Sarmah, B. Murali, I. Dursun, X.-H. Miao, A. L. Abdelhady, T. Wu, O. F. Mohammed and O. M. Bakr, *ACS Energy Lett.*, 2016, **1**, 32-37.
35. H. J. Snaith, *J. Phys. Chem. Lett.*, 2013, **4**, 3623-3630.
36. G. Wu, R. Fu, J. Chen, W. Yang, J. Ren, X. Guo, Z. Ni, X. Pi, C. Z. Li, H. Li and H. Chen, *Small*, 2018, **14**, 1802349.
37. C.-S. Liao, Q.-Q. Zhao, Y.-Q. Zhao, Z.-L. Yu, H. Zhou, P.-B. He, J.-L. Yang and M.-Q. Cai, *J. Phys. Chem. Solids*, 2019, **135**, 109060.
38. R. Ali, G.-J. Hou, Z.-G. Zhu, Q.-B. Yan, Q.-R. Zheng and G. Su, *Chem. Mater.*, 2018, **30**, 718-728.
39. Y. H. Kim, J. S. Kim and T. W. Lee, *Adv. Mater.*, 2019, **31**, 1804595.
40. M. Park, A. J. Neukirch, S. E. Reyes-Lillo, M. Lai, S. R. Ellis, D. Dietze, J. B. Neaton, P. Yang, S. Tretiak and R. A. Mathies, *Nat. Commun.*, 2018, **9**, 2525.
41. W.-J. Yin, H.-J. Gu and X.-G. Gong, in *Handbook of Materials Modeling*, 2019, DOI: 10.1007/978-3-319-50257-1_74-1, ch. Chapter 74-1, pp. 1-16.
42. D. J. Yang, Y. H. Du, Y. Q. Zhao, Z. L. Yu and M. Q. Cai, *Phys. Status Solidi b*, 2019, **256**, 1800540.
43. Y. Q. Zhao, Q. R. Ma, B. Liu, Z. L. Yu and M. Q. Cai, *Phys. Chem. Chem. Phys.*, 2018, **20**, 14718-14724.
44. F. Hao, C. C. Stoumpos, D. H. Cao, R. P. H. Chang and M. G. Kanatzidis, *Nat. Photonics*, 2014, **8**, 489-494.
45. N. K. Noel, S. D. Stranks, A. Abate, C. Wehrenfennig, S. Guarnera, A.-A. Haghighirad, A. Sadhanala, G. E. Eperon, S. K. Pathak, M. B. Johnston, A. Petrozza, L. M. Herz and H. J. Snaith, *Energy Environ. Sci.*, 2014, **7**, 3061-3068.
46. W. F. Yang, F. Igbari, Y. H. Lou, Z. K. Wang and L. S. Liao, *Adv. Energy Mater.*, 2019, DOI: 10.1002/aenm.201902584, 1902584.
47. L. N. Quan, M. Yuan, R. Comin, O. Voznyy, E. M. Beauregard, S. Hoogland, A. Buin, A. R. Kirmani, K. Zhao, A. Amassian, D. H. Kim and E. H. Sargent, *J. Am. Chem. Soc.*, 2016, **138**, 2649-2655.
48. F. Matteocci, L. Cinà, E. Lamanna, S. Cacovich, G. Divitini, P. A. Midgley, C. Ducati and A. Di Carlo, *Nano Energy*, 2016, **30**, 162-172.
49. H. C. Weerasinghe, Y. Dkhissi, A. D. Scully, R. A. Caruso and Y.-B. Cheng, *Nano Energy*, 2015, **18**, 118-125.
50. Y. Han, S. Meyer, Y. Dkhissi, K. Weber, J. M. Pringle, U. Bach, L. Spiccia and Y.-B. Cheng, *J. Matter. Chem. A*, 2015, **3**, 8139-8147.
51. S. Yang, Y. Wang, P. Liu, Y.-B. Cheng, H. J. Zhao and H. G. Yang, *Nat. Energy*, 2016, **1**, 15016.
52. C. Wu, D. Wang, Y. Zhang, F. Gu, G. Liu, N. Zhu, W. Luo, D. Han, X. Guo, B. Qu, S. Wang, Z. Bian, Z. Chen and L. Xiao, *Adv. Funct. Mater.*, 2019, **29**, 1902974.
53. D. Bi, P. Gao, R. Scopelliti, E. Oveisi, J. Luo, M. Grätzel, A. Hagfeldt and M. K. Nazeeruddin, *Adv. Mater.*, 2016, **28**, 2910-2915.
54. J. Zhang, Z. Hu, L. Huang, G. Yue, J. Liu, X. Lu, Z. Hu, M. Shang, L. Han and Y. Zhu, *Chem. Commun. (Camb)*, 2015, **51**, 7047-7050.
55. J. Cao, J. Yin, S. Yuan, Y. Zhao, J. Li and N. Zheng, *Nanoscale*, 2015, **7**, 9443-9447.
56. L. Mao, W. Ke, L. Pedesseau, Y. Wu, C. Katan, J. Even, M. R. Wasielewski, C. C. Stoumpos and M. G. Kanatzidis, *J. Am. Chem. Soc.*, 2018, **140**, 3775-3783.
57. W. Ke, L. Mao, C. C. Stoumpos, J. Hoffman, I. Spanopoulos, A. D. Mohite and M. G. Kanatzidis, *Adv. Energy Mater.*, 2019, **9**, 1803384.
58. Z. Xu, M. Chen and S. F. Liu, *J. Phys. Chem. Lett.*, 2019, **10**, 3670-3675.
59. Y. Zheng, T. Niu, J. Qiu, L. Chao, B. Li, Y. Yang, Q. Li, C. Lin, X. Gao, C. Zhang, Y. Xia, Y. Chen and W. Huang, *Solar RRL*, 2019, **3**, 1900090.
60. F. Wei, Z. Deng, S. Sun, F. Xie, G. Kieslich, D. M. Evans, M. A. Carpenter, P. D. Bristowe and A. K. Cheetham, *Mater. Horiz.*, 2016, **3**, 328-332.
61. F. Wei, Z. Deng, S. Sun, F. Zhang, D. M. Evans, G. Kieslich, S. Tominaka, M. A. Carpenter, J. Zhang, P. D. Bristowe and A. K. Cheetham, *Chem. Mater.*, 2017, **29**, 1089-1094.
62. Y.-J. Li, T. Wu, L. Sun, R.-X. Yang, L. Jiang, P.-F. Cheng, Q.-Q. Hao, T.-J. Wang, R.-F. Lu and W.-Q. Deng, *RSC Advances*, 2017, **7**, 35175-35180.
63. Z. Deng, F. Wei, F. Brivio, Y. Wu, S. Sun, P. D. Bristowe and A. K. Cheetham, *J. Phys. Chem. Lett.*, 2017, **8**, 5015-5020.
64. Z. Deng, F. Wei, S. Sun, G. Kieslich, A. K. Cheetham and P. D. Bristowe, *J. Matter. Chem. A*, 2016, **4**, 12025-12029.
65. C. Liang, D. Zhao, Y. Li, X. Li, S. Peng, G. Shao and G. Xing, *Energ. Environ. Matter.*, 2018, **1**, 221-231.
66. H. Zheng, G. Liu, L. Zhu, J. Ye, X. Zhang, A. Alsaedi, T. Hayat, X. Pan and S. Dai, *Adv. Energy Mater.*, 2018, **8**, 1800051.
67. I. C. Smith, E. T. Hoke, D. Solis-Ibarra, M. D. McGehee and H. I. Karunadasa, *Angew. Chem. Int. Ed. Engl.*, 2014, **53**, 11232-11235.
68. D. H. Cao, C. C. Stoumpos, O. K. Farha, J. T. Hupp and M. G. Kanatzidis, *J. Am. Chem. Soc.*, 2015, **137**, 7843-7850.
69. R. L. Milot, R. J. Sutton, G. E. Eperon, A. A. Haghighirad, J. Martinez Hardigree, L. Miranda, H. J. Snaith, M. B. Johnston and L. M. Herz, *Nano Lett.*, 2016, **16**, 7001-7007.
70. Y. Q. Zhao, Q. R. Ma, B. Liu, Z. L. Yu, J. Yang and M. Q. Cai, *Nanoscale*, 2018, **10**, 8677-8688.
71. Y.-F. Ding, Q.-Q. Zhao, Z.-L. Yu, Y.-Q. Zhao, B. Liu, P.-B. He, H. Zhou, K. Li, S.-F. Yin and M.-Q. Cai, *J. Matter. Chem. C*, 2019, **7**, 7433-7441.
72. N. A. Benedek and C. J. Fennie, *J. Phys. Chem. C*, 2013, **117**, 13339-13349.
73. P. S. Halasyamani, *Chem. Mater.*, 2004, **16**, 3586-3592.
74. N. A. Benedek, A. T. Mulder and C. J. Fennie, *J. Solid State Chem.*, 2012, **195**, 11-20.
75. T. J. Jacobsson, M. Pazoki, A. Hagfeldt and T. Edvinsson, *J. Phys. Chem. C*, 2015, **119**, 25673-25683.
76. V. M. Goldschmidt, *Die Naturwissenschaften*, 1926, **14**, 477-485.
77. N. K. McKinnon, D. C. Reeves and M. H. Akabas, *J. Gen. Physiol.*, 2011, **138**, 453-466.
78. Y. Dang, Y. Liu, Y. Sun, D. Yuan, X. Liu, W. Lu, G. Liu, H. Xia and X. Tao, *CrystEngComm*, 2015, **17**, 665-670.
79. S. N. Ruddlesden and P. Popper, *Acta Cryst.*, 1957, **10**, 538-539.
80. D. Lee and H. N. Lee, *Materials (Basel)*, 2017, **10**, 368.
81. C. C. Stoumpos, D. H. Cao, D. J. Clark, J. Young, J. M.

Rondinelli, J. I. Jang, J. T. Hupp and M. G. Kanatzidis, *Chem. Mater.*, 2016, **28**, 2852-2867.
82. X. Hong, T. Ishihara and A. V. Nurmikko, *Phys. Rev. B*, 1992, **45**, 6961-6964.
83. H. Xu, Y. Jiang, T. He, S. Li, H. Wang, Y. Chen, M. Yuan and J. Chen, *Adv. Funct. Mater.*, 2019, **29**, 1807696.
84. C. Zhao, W. Tian, J. Leng, Y. Zhao and S. Jin, *J. Phys. Chem. Lett.*, 2019, **10**, 3950-3954.
85. S. Zhang, S. M. Hosseini, R. Gunder, A. Petsiuk, P. Caprioglio, C. M. Wolff, S. Shoaee, P. Meredith, S. Schorr, T. Unold, P. L. Burn, D. Neher and M. Stolterfoht, *Adv. Mater.*, 2019, **31**, 1901090.
86. Q. Zhang, A. Solanki, K. Parida, D. Giovanni, M. Li, T. L. C. Jansen, M. S. Pshenichnikov and T. C. Sum, *ACS Appl. Mater. Inter.*, 2019, **11**, 13523-13532.
87. P. Vashishtha, M. Ng, S. B. Shivarudraiah and J. E. Halpert, *Chem. Mater.*, 2018, **31**, 83-89.
88. I. Spanopoulos, I. Hadar, W. Ke, Q. Tu, M. Chen, H. Tsai, Y. He, G. Shekhawat, V. P. Dravid, M. R. Wasielewski, A. D. Mohite, C. C. Stoumpos and M. G. Kanatzidis, *J. Am. Chem. Soc.*, 2019, **141**, 5518-5534.
89. S. Yang, W. Niu, A. L. Wang, Z. Fan, B. Chen, C. Tan, Q. Lu and H. Zhang, *Angew. Chem. Int. Ed. Engl.*, 2017, **56**, 4252-4255.
90. J. Chen, L. Gan, F. Zhuge, H. Li, J. Song, H. Zeng and T. Zhai, *Angew. Chem. Int. Ed. Engl.*, 2017, **56**, 2390-2394.
91. X. Duan, C. Wang, A. Pan, R. Yu and X. Duan, *Chem. Soc. Rev.*, 2015, **44**, 8859-8876.
92. Y. Liu, N. O. Weiss, X. Duan, H.-C. Cheng, Y. Huang and X. Duan, *Nat. Rev. Mater.*, 2016, **1**, 16042.
93. K. S. Novoselov, A. Mishchenko, A. Carvalho and A. H. Castro Neto, *Science*, 2016, **353**, aac9439.
94. R. Yan, D. Gargas and P. Yang, *Nat. Photonics*, 2009, **3**, 569-576.
95. Y. Wang, Y. Shi, G. Xin, J. Lian and J. Shi, *Cryst. Growth Des.*, 2015, **15**, 4741-4749.
96. Z. Chen, Y. Wang, Y. Shi, B. Hsu, Z. Yang and J. Shi, *Adv. Electron. Matter.*, 2016, **2**, 1600248.
97. Z. Chen, Y. Wang, X. Sun, Y. Guo, Y. Hu, E. Wertz, X. Wang, H. Gao, T.-M. Lu and J. Shi, *Adv. Opt. Matter.*, 2017, **5**, 1700373.
98. Y. Hu, Y. Guo, Y. Wang, Z. Chen, X. Sun, J. Feng, T.-M. Lu, E. Wertz and J. Shi, *J. Mater. Res.*, 2017, **32**, 3992-4024.
99. J. Wang, J. Li, Q. Tan, L. Li, J. Zhang, J. Zang, P. Tan, J. Zhang and D. Li, *J. Phys. Chem. Lett.*, 2017, **8**, 6211-6219.
100. Y. Wang, Z. Chen, F. Deschler, X. Sun, T. M. Lu, E. A. Wertz, J. M. Hu and J. Shi, *ACS Nano*, 2017, **11**, 3355-3364.
101. Z. Chen, Y. Wang, X. Sun, Y. Xiang, Y. Hu, J. Jiang, J. Feng, Y. Y. Sun, X. Wang, G. C. Wang, T. M. Lu, H. Gao, E. A. Wertz and J. Shi, *J. Phys. Chem. Lett.*, 2018, **9**, 6676-6682.
102. Y. Wang, L. Gao, Y. Yang, Y. Xiang, Z. Chen, Y. Dong, H. Zhou, Z. Cai, G.-C. Wang and J. Shi, *Phys, Rev. Mater.*, 2018, **2**, 076002.
103. Z. Chen, Y. Guo, E. Wertz and J. Shi, *Adv. Mater.*, 2019, **31**, 11803514.
104. J. Jiang, X. Sun, X. Chen, B. Wang, Z. Chen, Y. Hu, Y. Guo, L. Zhang, Y. Ma, L. Gao, F. Zheng, L. Jin, M. Chen, Z. Ma, Y. Zhou, N. P. Padture, K. Beach, H. Terrones, Y. Shi, D. Gall, T. M. Lu, E. Wertz, J. Feng and J. Shi, *Nat. Commun.*, 2019, **10**, 4145.
105. J. Wang, J. Li, S. Lan, C. Fang, H. Shen, Q. Xiong and D. Li, *ACS Nano*, 2019, **13**, 5473-5484.
106. J. Wang, Y. Mi, X. Gao, J. Li, J. Li, S. Lan, C. Fang, H. Shen, X. Wen, R. Chen, X. Liu, T. He and D. Li, *Adv. Opt. Matter.*, 2019, **7**, 1900398.
107. M. Era, T. Hattori, T. Taira and T. Tsutsui, *Chem. Mater.*, 1997, **9**, 8-10.
108. W. Niu, A. Eiden, G. Vijaya Prakash and J. J. Baumberg, *Appl. Phys. Lett.*, 2014, **104**, 171111.
109. O. Yaffe, A. Chernikov, Z. M. Norman, Y. Zhong, A. Velauthapillai, A. van der Zande, J. S. Owen and T. F. Heinz, *Phys. Rev. B*, 2015, **92**, 045414.
110. X. Wu, M. T. Trinh, D. Niesner, H. Zhu, Z. Norman, J. S. Owen, O. Yaffe, B. J. Kudisch and X. Y. Zhu, *J. Am. Chem. Soc.*, 2015, **137**, 2089-2096.
111. Z. Guo, X. Wu, T. Zhu, X. Zhu and L. Huang, *ACS Nano*, 2016, **10**, 9992-9998.
112. V. A. Hintermayr, A. F. Richter, F. Ehrat, M. Doblinger, W. Vanderlinden, J. A. Sichert, Y. Tong, L. Polavarapu, J. Feldmann and A. S. Urban, *Adv. Mater.*, 2016, **28**, 9478-9485.
113. J. Li, J. Wang, Y. Zhang, H. Wang, G. Lin, X. Xiong, W. Zhou, H. Luo and D. Li, *2D Matter.*, 2018, **5**, 021001.
114. W. J. Wei, X. X. Jiang, L. Y. Dong, W. W. Liu, X. B. Han, Y. Qin, K. Li, W. Li, Z. S. Lin, X. H. Bu and P. X. Lu, *J. Am. Chem. Soc.*, 2019, **141**, 9134-9139.
115. L. Li, Z. Sun, P. Wang, W. Hu, S. Wang, C. Ji, M. Hong and J. Luo, *Angew. Chem. Int. Ed. Engl.*, 2017, **56**, 12150-12154.
116. K. Leng, I. Abdelwahab, I. Verzhbitskiy, M. Telychko, L. Chu, W. Fu, X. Chi, N. Guo, Z. Chen, Z. Chen, C. Zhang, Q. H. Xu, J. Lu, M. Chhowalla, G. Eda and K. P. Loh, *Nat. Mater.*, 2018, **17**, 908-914.
117. Y. Dang, J. Wei, X. Liu, X. Wang, K. Xu, M. Lei, W. Hu and X. Tao, *Sustain. Energ. Fuels*, 2018, **2**, 2237-2243.
118. Z. Xu, Y. Li, X. Liu, C. Ji, H. Chen, L. Li, S. Han, M. Hong, J. Luo and Z. Sun, *Adv. Opt. Matter.*, 2019, **7**, 1900308.
119. J.-W. Lee, S.-H. Bae, N. De Marco, Y.-T. Hsieh, Z. Dai and Y. Yang, *Mater. Today Energy*, 2018, **7**, 149-160.
120. C. M. Raghavan, T. P. Chen, S. S. Li, W. L. Chen, C. Y. Lo, Y. M. Liao, G. Haider, C. C. Lin, C. C. Chen, R. Sankar, Y. M. Chang, F. C. Chou and C. W. Chen, *Nano Lett.*, 2018, **18**, 3221-3228.
121. H. Tian, L. Zhao, X. Wang, Y. W. Yeh, N. Yao, B. P. Rand and T. L. Ren, *ACS Nano*, 2017, **11**, 12247-12256.
122. Y. Liu, H. Ye, Y. Zhang, K. Zhao, Z. Yang, Y. Yuan, H. Wu, G. Zhao, Z. Yang, J. Tang, Z. Xu and S. Liu, *Matter*, 2019, **1**, 465-480.
123. Y. Dang, D. Ju, L. Wang and X. Tao, *CrystEngComm*, 2016, **18**, 4476-4484.
124. Y. Dang, Y. Zhou, X. Liu, D. Ju, S. Xia, H. Xia and X. Tao, *Angew. Chem. Int. Ed. Engl.*, 2016, **55**, 3447-3450.
125. Y. Liu, Z. Yang, D. Cui, X. Ren, J. Sun, X. Liu, J. Zhang, Q. Wei, H. Fan, F. Yu, X. Zhang, C. Zhao and S. F. Liu, *Adv. Mater.*, 2015, **27**, 5176-5183.
126. Y. Liu, Z. Yang and S. F. Liu, *Adv. Sci. (Weinh)*, 2018, **5**, 1700471.
127. F. Lédée, G. Trippé-Allard, H. Diab, P. Audebert, D. Garrot, J.-S. Lauret and E. Deleporte, *CrystEngComm*, 2017, **19**, 2598-2602.
128. D. Ma, Y. Fu, L. Dang, J. Zhai, I. A. Guzei and S. Jin, *Nano Res.*, 2017, **10**, 2117-2129.
129. W. Peng, J. Yin, K. T. Ho, O. Ouellette, M. De Bastiani, B. Murali, O. El Tall, C. Shen, X. Miao, J. Pan, E. Alarousu, J. H.

He, B. S. Ooi, O. F. Mohammed, E. Sargent and O. M. Bakr, *Nano Lett.*, 2017, **17**, 4759-4767.
130. K. Wang, C. Wu, D. Yang, Y. Jiang and S. Priya, *ACS Nano*, 2018, **12**, 4919-4929.
131. G. Kieslich, S. Sun and A. K. Cheetham, *Chem. Sci.*, 2015, **6**, 3430-3433.
132. W. S. Yang, J. H. Noh, N. J. Jeon, Y. C. Kim, S. Ryu, J. Seo and S. I. Seok, *Science*, 2015, **348**, 1234-1237.
133. Z. Tan, Y. Wu, H. Hong, J. Yin, J. Zhang, L. Lin, M. Wang, X. Sun, L. Sun, Y. Huang, K. Liu, Z. Liu and H. Peng, *J. Am. Chem. Soc.*, 2016, **138**, 16612-16615.
134. X. Wang, P. Wang, J. Wang, W. Hu, X. Zhou, N. Guo, H. Huang, S. Sun, H. Shen, T. Lin, M. Tang, L. Liao, A. Jiang, J. Sun, X. Meng, X. Chen, W. Lu and J. Chu, *Adv. Mater.*, 2015, **27**, 6575-6581.
135. V. M. Fridkin, *Photoferroelectrics*, 1979.
136. S. Wang, L. Li, W. Weng, C. Ji, X. Liu, Z. Sun, W. Lin, M. Hong and J. Luo, *J. Am. Chem. Soc.*, 2020, **142**, 55-59.
137. L. Li, X. Liu, Y. Li, Z. Xu, Z. Wu, S. Han, K. Tao, M. Hong, J. Luo and Z. Sun, *J. Am. Chem. Soc.*, 2019, **141**, 2623-2629.
138. Y. Wang, R. Fullon, M. Acerce, C. E. Petoukhoff, J. Yang, C. Chen, S. Du, S. K. Lai, S. P. Lau, D. Voiry, D. O'Carroll, G. Gupta, A. D. Mohite, S. Zhang, H. Zhou and M. Chhowalla, *Adv. Mater.*, 2017, **29**, 1603995.
139. Y. Lee, J. Kwon, E. Hwang, C. H. Ra, W. J. Yoo, J. H. Ahn, J. H. Park and J. H. Cho, *Adv. Mater.*, 2015, **27**, 41-46.
140. J. Song, L. Xu, J. Li, J. Xue, Y. Dong, X. Li and H. Zeng, *Adv. Mater.*, 2016, **28**, 4861-4869.
141. J. Xue, Y. Gu, Q. Shan, Y. Zou, J. Song, L. Xu, Y. Dong, J. Li and H. Zeng, *Angew. Chem. Int. Ed. Engl.*, 2017, **56**, 5232-5236.
142. X. Liu, S. Wang, P. Long, L. Li, Y. Peng, Z. Xu, S. Han, Z. Sun, M. Hong and J. Luo, *Angew. Chem. Int. Ed. Engl.*, 2019, **58**, 14504-14508.
143. J. Feng, C. Gong, H. Gao, W. Wen, Y. Gong, X. Jiang, B. Zhang, Y. Wu, Y. Wu, H. Fu, L. Jiang and X. Zhang, *Nat. Electron.*, 2018, **1**, 404-410.
144. K. Wang, C. Wu, Y. Jiang, D. Yang, K. Wang and S. Priya, *Sci. Adv.*, 2019, **5**, eaau3241.
145. R. Dong, C. Lan, X. Xu, X. Liang, X. Hu, D. Li, Z. Zhou, L. Shu, S. Yip, C. Li, S. W. Tsang and J. C. Ho, *ACS Appl. Mater. Inter.*, 2018, **10**, 19019-19026.
146. D. Yu, F. Cao, Y. Shen, X. Liu, Y. Zhu and H. Zeng, *J. Phys. Chem. Lett.*, 2017, **8**, 2565-2572.
147. L. Ke, X. Gan, W. Zhao, L. Guo and H. Liu, *J. Alloys Compd.*, 2019, **788**, 954-960.
148. H. Zheng, G. Liu, X. Xu, X. Zhang, A. Alsaedi, T. Hayat and X. Pan, *ACS Sustain. Chem. Eng.*, 2018, **6**, 15143-15150.
149. H. Zhang, Y. Wu, Q. Liao, Z. Zhang, Y. Liu, Q. Gao, P. Liu, M. Li, J. Yao and H. Fu, *Angew. Chem. Int. Ed. Engl.*, 2018, **57**, 7748-7752.
150. R. Dong, C. Lan, F. Li, S. Yip and J. C. Ho, *Nanoscale Horiz.*, 2019, **4**, 1342-1352.
151. C. Fang, H. Wang, Z. Shen, H. Shen, S. Wang, J. Ma, J. Wang, H. Luo and D. Li, *ACS Appl. Mater. Inter.*, 2019, **11**, 8419-8427.
152. B. V. Lotsch, *Annu. Rev. Mater. Res.*, 2015, **45**, 85-109.
153. M. Liu, M. B. Johnston and H. J. Snaith, *Nature*, 2013, **501**, 395-398.
154. Q. Chen, H. Zhou, Z. Hong, S. Luo, H. S. Duan, H. H. Wang, Y. Liu, G. Li and Y. Yang, *J. Am. Chem. Soc.*, 2014, **136**, 622-625.
155. P. W. Liang, C. Y. Liao, C. C. Chueh, F. Zuo, S. T. Williams, X. K. Xin, J. Lin and A. K. Jen, *Adv. Mater.*, 2014, **26**, 3748-3754.
156. Z. X. Zhang, Z. Long-Hui, X. W. Tong, Y. Gao, C. Xie, Y. H. Tsang, L. B. Luo and Y. C. Wu, *J. Phys. Chem. Lett.*, 2018, **9**, 1185-1194.
157. K.-H. Hu, Z.-K. Wang, L. Meng, K.-L. Wang, Y. Zhang and L.-S. Liao, *J. Matter. Chem. C*, 2019, **7**, 6391-6397.
158. Y. Chen, Y. Sun, J. Peng, J. Tang, K. Zheng and Z. Liang, *Adv. Mater.*, 2018, **30**, 1703487.
159. J. Zhou, Y. Chu and J. Huang, *ACS Appl. Mater. Inter.*, 2016, **8**, 25660-25666.
160. J. Chen, Y. Wang, L. Gan, Y. He, H. Li and T. Zhai, *Angew. Chem. Int. Ed. Engl.*, 2017, **56**, 14893-14897.
161. L. Li, L. Jin, Y. Zhou, J. Li, J. Ma, S. Wang, W. Li and D. Li, *Adv. Opt. Matter.*, 2019, **7**, 1900988.
162. S. Han, P. Wang, J. Zhang, X. Liu, Z. Sun, X. Huang, L. Li, C. Ji, W. Zhang, B. Teng, W. Hu, M. Hong and J. Luo, *Laser Photonics Rev.*, 2018, **12**, 1800060.
163. Y. Yan, Q. Wu, Y. Zhao, S. Chen, S. Hu, J. Zhu, J. Huang and Z. Liang, *Small*, 2018, **14**, 1802764.
164. X. He, Y. Wang, K. Li, X. Wang, P. Liu, Y. Yang, Q. Liao, T. Zhai, J. Yao and H. Fu, *ACS Appl. Mater. Inter.*, 2019, **11**, 15905-15912.
165. J. Lu, A. Carvalho, H. Liu, S. X. Lim, A. H. Castro Neto and C. H. Sow, *Angew. Chem. Int. Ed. Engl.*, 2016, **55**, 11945-11949.
166. F. Bai, J. Qi, F. Li, Y. Fang, W. Han, H. Wu and Y. Zhang, *Adv. Mater. Interfaces*, 2018, **5**, 1701275.
167. C. Ma, Y. Shi, W. Hu, M. H. Chiu, Z. Liu, A. Bera, F. Li, H. Wang, L. J. Li and T. Wu, *Adv. Mater.*, 2016, **28**, 3683-3689.

View Article Online
DOI: 10.1039/C9SE01181A

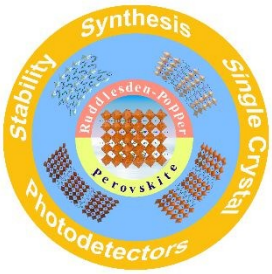

This review presents the progress of the synthesis, single crystal growth, enhanced stability, and applications as high-performance photodetectors.